



RESEARCH ARTICLE

10.1002/2016GC006656

Upper mantle structure of the Tonga-Lau-Fiji region from Rayleigh wave tomography

S. Shawn Wei^{1,2}, Yang Zha³, Weisen Shen¹, Douglas A. Wiens¹, James A. Conder⁴, and Spahr C. Webb³

Key Points:

- Low velocities beneath the Lau Basin show along-strike variations of mantle melt porosity and the interactions between arc and back-arc
- The Fiji Plateau-Lau Ridge, except the northeastern part, is underlain by a 60–80 km thick ancient arc lithosphere
- Spreading-perpendicular anisotropy beneath the Lau Basin supports the southward flow in the Tonga mantle wedge

Supporting Information:

- Supporting Information S1

Correspondence to:

S. S. Wei,
shawnwei@ucsd.edu

Citation:

Wei, S. S., Y. Zha, W. Shen, D. A. Wiens, J. A. Conder, and S. C. Webb (2016), Upper mantle structure of the Tonga-Lau-Fiji region from Rayleigh wave tomography, *Geochem. Geophys. Geosyst.*, 17, doi:10.1002/2016GC006656.

Received 22 SEP 2016

Accepted 28 OCT 2016

Accepted article online 7 NOV 2016

¹Department of Earth and Planetary Sciences, Washington University, St. Louis, Missouri, USA, ²Now at Institute of Geophysics and Planetary Physics, Scripps Institution of Oceanography, University of California, San Diego, La Jolla, California, USA, ³Lamont-Doherty Earth Observatory, Columbia University, Palisades, New York, USA, ⁴Department of Geology and Geophysics, Southern Illinois University, Carbondale, Illinois, USA

Abstract We investigate the upper mantle seismic structure in the Tonga-Lau-Fiji region by jointly fitting the phase velocities of Rayleigh waves from ambient-noise and two-plane-wave tomography. The results suggest a wide low-velocity zone beneath the Lau Basin, with a minimum *SV*-velocity of about 3.7 ± 0.1 km/s, indicating upwelling hot asthenosphere with extensive partial melting. The variations of velocity anomalies along the Central and Eastern Lau Spreading Centers suggest varying mantle porosity filled with melt. In the north where the spreading centers are distant from the Tonga slab, the inferred melting commences at about 70 km depth, and forms an inclined zone in the mantle, dipping to the west away from the arc. This pattern suggests a passive decompression melting process supplied by the Australian plate mantle from the west. In the south, as the supply from the Australian mantle is impeded by the Lau Ridge lithosphere, flux melting controlled by water from the nearby slab dominates in the back-arc. This source change results in the rapid transition in geochemistry and axial morphology along the spreading centers. The remnant Lau Ridge and the Fiji Plateau are characterized by a 60–80 km thick lithosphere underlain by a low-velocity asthenosphere. Our results suggest the removal of the lithosphere of the northeastern Fiji Plateau-Lau Ridge beneath the active Taveuni Volcano. Azimuthal anisotropy shows that the mantle flow direction rotates from trench-perpendicular beneath Fiji to spreading-perpendicular beneath the Lau Basin, which provides evidence for the southward flow of the mantle wedge and the Samoan plume.

1. Introduction

Back-arc spreading centers are usually compared with mid-ocean ridges (MORs) due to the similar tectonic spreading mechanisms and overall structure. However, because of the significant influence of the adjacent subduction process, back-arc spreading centers are different from the MORs in geomorphological, geophysical, and geochemical perspectives [e.g., Taylor et al., 1996; Zhao et al., 1997; Kelley et al., 2006]. The Lau back-arc basin and the adjacent areas are exemplary locations for understanding the interactions between the back-arc spreading and the subduction processes. While the Pacific Plate subducts along the Tonga Trench beneath the Australian Plate, new oceanic crust is generated at the back-arc spreading centers in the Lau Basin (Figure 1a). One may expect the water and other materials released from the slab to enter the melting region beneath the back-arc, and then return to the surface with the melt. Detailed seismic images of the mantle wedge, sensitive to temperature and volatile contents, are necessary to provide direct evidence and constraints on these interactions.

Along the Central (CLSC) and Eastern Lau (ELSC) Spreading centers, the distance from the spreading center to the trench decreases from north to south along with the spreading rate. This variation in distance appears to cause systematic variations in the geological features of the spreading centers due to the changes in degree of interaction between arc and back-arc [Martinez and Taylor, 2002]. The CLSC, 160–185 km from the volcanic arc, is characterized by a normal crustal thickness of 6–7 km, shallow bathymetry, fast spreading rates of 85–95 mm/yr, and mid-ocean ridge basalt (MORB)-like geochemical features. To the south, the ELSC, 60–110 km from the arc, has a thin crust, deep axial bathymetry, and intermediate spreading rates of 60–95 mm/yr. Lavas from the ELSC are strongly depleted compared to MORB, and their arc geochemical signature is weaker than found further south along the Valu Fa Ridge (VFR). The VFR, only

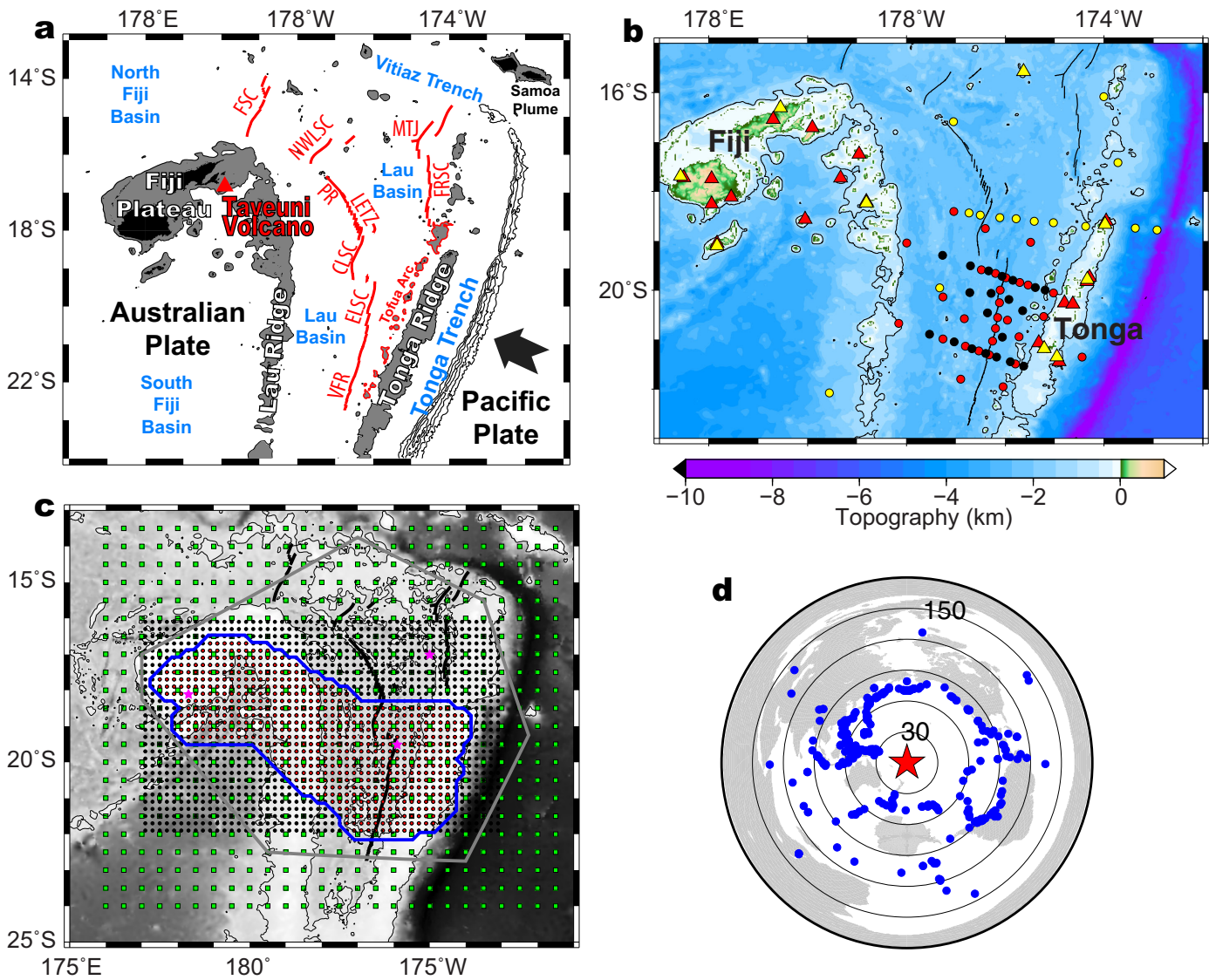


Figure 1. Maps of the Tonga-Lau-Fiji region. (a) Tectonic map of the Lau Basin and adjacent areas with back-arc spreading centers (red curves). The Pacific Plate subducts beneath the Tonga Trench (delineated by bathymetric contours of 7, 8, 9, and 10 km) from the southeast (bold arrow). Areas with bathymetry shallower than 1 and 0 km are shaded in gray and black, respectively. Features with active magmatism are labeled in red. CLSC, Central Lau Spreading Center; ELSC, East Lau Spreading Center; LETZ, Lau Extensional Transform Zone; FRSC, Fonualei Rift and Spreading Center; FSC, Futuna Spreading Center; MTJ, Mangatolu Triple Junction; and VFR, Valu Fa Ridge. (b) Seismic stations used in this study. Red triangles represent island-based stations operated from October 2009 to December 2010. Red and black dots are WHOI and LDEO OBSs deployed from November 2009 to November 2010, respectively. Yellow dots and triangles indicate OBSs and island-based stations deployed during September to December 1994, respectively. Spreading centers are denoted by black curves, and the 1 km bathymetric contours are shown. (c) Nodes for SV-wave velocity inversion. Green dots represent the nodes for the TPWT, black dots indicated the ANT nodes, and red dots included by the blue contour are the nodes for the ANT-TPWT joint inversion. The gray polygon outlines the region in which we display the TPWT inversion because within it we achieved a reasonable resolution of phase-velocity inversion at all periods (supporting information Figure S3). The region in which the ANT is performed slightly varies with respect to period. We thus design a region for the joint ANT-TPWT inversion (blue contour) so that all nodes within it have well-resolved phase velocities at more than 5 periods from the ANT. Magenta stars illustrate nodes used as examples shown in Figure 4. (d) Earthquakes (blue dots) used in this study centered at the Lau Basin (red star).

40–60 km from the arc, is characterized by a thick crust (7.5–9 km thick), shallow bathymetry, slower spreading rates of 40–60 mm/yr, and the primarily arc-like compositions of its rocks [Pearce et al., 1994; Turner et al., 1999; Zellmer and Taylor, 2001; Martinez and Taylor, 2002; Crawford et al., 2003]. This distance-controlling hypothesis explains the along-strike variations as the result of increasing input of subduction-related materials southward [Martinez and Taylor, 2002], though direct evidence from seismic imaging is needed.

More recent studies of geochemistry and geophysics in this region reveal additional complexities, at smaller scales, beyond the distance-controlling hypothesis. Bathymetric surveys indicate that the spreading center

becomes flatter and more faulted when the spreading rate increases, which is opposite to the usual trend at MORs [Martinez *et al.*, 2006]. Although the distance from the spreading centers to the arc decreases southward gradually, Mg# and trace element concentrations (e.g., Ba, Th, and La) of the lavas show abrupt transitions at latitudes of about 20.6°S and 21.2°S [Escrig *et al.*, 2009], which coincides with the transitions of the axial morphology from the northern ELSC to the central ELSC and the central ELSC to the VFR, respectively [Martinez *et al.*, 2006]. In addition, the crustal and mantle structures of the Fiji Plateau and the Lau Ridge are poorly known [e.g., Dubois *et al.*, 1973]. Although most geochemical evidence shows a signature of the Samoan plume in the northern Lau Basin [e.g., Wendt *et al.*, 1997; Turner and Hawkesworth, 1998], studies of the Fijian volcanoes and the back-arc spreading centers in the northwestern Lau Basin imply more complexities in terms of mantle source materials [Gill and Whelan, 1989; Lytle *et al.*, 2012; Price *et al.*, 2014]. A detailed seismic model for the Fiji Plateau is essential to address these problems.

Previous passive broadband seismological studies in this region mainly consist of the Southwest Pacific Seismic Experiment (SPASE) (November 1993 to December 1995) and the Lau Basin ocean-bottom seismograph survey (LABATTS) (September 1994 to December 1994). Body wave tomography showed a region with low seismic velocities [Zhao *et al.*, 1997; Conder and Wiens, 2006] and high attenuation [Roth *et al.*, 1999] in the uppermost mantle beneath the CLSC, which has an asymmetric shape dipping westward. Shear wave splitting results suggested that mantle flow is parallel to the convergence direction beneath the Fiji Plateau, and rotates perpendicular to the convergence direction with increasing proximity to the trench [Smith *et al.*, 2001]. However, since most of the seismic stations in these two experiments were deployed along a linear profile across the Tonga Ridge, the CLSC, and the Fiji Plateau, the previous studies were not able to demonstrate E-W striking variations or complex 3-D patterns. In particular, the changes along the spreading centers and the characteristics of the Fiji Plateau were not fully addressed.

The Ridge2000 Lau Spreading Center Imaging project in 2009–2010 provided high quality seismic data to help us better understand the N-S variations. The 3-D active source seismic survey showed that the abrupt changes in geomorphology and geochemistry along the ELSC-VFR correspond with a rapid transition southward from typical oceanic crust to an abnormally porous and hydrous crust. This transition implies a much larger influence of subduction zone water in sections that are closer to the arc [Dunn and Martinez, 2011; Dunn *et al.*, 2013; Arai and Dunn, 2014]. Ambient-noise tomography further supported this idea by directly imaging the connection between the back-arc and arc melting regions beneath the VFR [Zha *et al.*, 2014]. Moreover, the Rayleigh wave tomography using teleseismic data emphasized the melt extraction rate, influenced by the water released from the slab, as one of the crucial factors in controlling the magmatism in the Lau Basin [Wei *et al.*, 2015].

Although Zha *et al.* [2014] inverted for the *S*-wave velocity structures of the Lau Basin using ambient-noise tomographic methods (ANT) and Wei *et al.* [2015] inverted teleseismic Rayleigh waves at long periods using two-plane-wave tomography method [Forsyth and Li, 2005; Yang and Forsyth, 2006] (TPWT), no study has investigated the dispersion curves over the entire range of observable periods. Both methods provide structural information in complementary period bands: ANT inverts phase velocities at periods from 8 to 18 s, most sensitive to about 10–25 km depths, whereas TPWT inverts those from 23 to 88 s, most sensitive to about 30–140 km depths. Inverting the entire observable dispersion curve can greatly improve the resolution at intermediate depths (25–35 km), where the interactions between the arc and back-arc magmatism are expected to be most intense. Additionally, the structures of the Lau Ridge, Fiji Plateau, and the Tofua arc have not been investigated in detail. In this study, we present new measurements of azimuthal anisotropy of Rayleigh waves and of *S*-wave velocity structure by jointly inverting from phase velocities determined using both ANT and TPWT methods. In the light of our *S*-wave velocity structure as well as previous studies, we construct a comprehensive model of the upper mantle for Tonga, Lau, Fiji, and the adjacent regions.

2. Data and Methods

2.1. Data Collection

Most of the data used in the phase-velocity inversion was collected from 49 ocean bottom seismographs (OBSs) deployed from November 2009 to November 2010 (red and black dots in Figure 1b) and 17 island-based seismic stations operated from October 2009 to December 2010 (red triangles in Figure 1b). The OBS array consisted of two profiles that are approximately arc-perpendicular extending across the ELSC to the

active Tofua arc, one profile along the ELSC between the two main profiles, and a sparse 2-D array surrounding the profiles. Each OBS from Woods Hole Oceanographic Institution (WHOI) contains a Guralp CMG3T seismometer and a Quanterra Q330 datalogger, while the other OBSs from Lamont-Doherty Earth Observatory (LDEO) use modified Sercel (formerly Mark Products) L-4C seismometers and LDEO-designed dataloggers. The land stations were deployed on various islands in Tonga and Fiji. Each of them consists of a broadband three-component seismometer (Guralp CMG3T or Streckeisen STS-2 or Nanometrics Trillium 120PA) and a Reftek 130-01 recorder. We additionally used earthquake Rayleigh wave data from 14 OBSs from the LABATTS experiment and 9 island-based broadband stations from the SPASE project [Koper *et al.*, 1998] collected from September to December 1994 for the TPWT.

2.2. Phase-Velocity Inversion: Ambient Noise Cross-Correlation

The ANT analysis was similar to Zha *et al.* [2014] using the frequency-domain method of Ekström *et al.* [2009], but we additionally included data from land stations in this study. The daily vertical component seismograms were first quality controlled, corrected for clock drift and instrument response, down-sampled to 5 samples per second (sps), cut into 100 overlapping windows, and then Fourier-transformed into the frequency domain. A correlation spectrum between each station pair was normalized by the spectral amplitudes, averaged over all windows in a day, and stacked over all days. This frequency-domain normalization for each short time window effectively removes the effects of large earthquakes.

We calculated phase velocities using the zero-crossing of the averaged correlation spectra to generate a suite of possible dispersion curves [Ekström *et al.*, 2009]. In order to extract the most reasonable dispersion curve, we used previous results for the crustal structure [Crawford *et al.*, 2003] and a V_p/V_s ratio of 1.85 [Conder and Wiens, 2006] to generate a reference dispersion curve. For each station pair, the average water depth was used to adjust the reference model before calculating the dispersion curve. Since water depth greatly affects Rayleigh wave phase velocity at short periods (<10 s), we discarded dispersion curves between OBS stations that have bathymetry differences greater than 1 km. No elevation restriction was applied to land-land or land-OBS pairs due to their better quality of dispersion curves. All dispersion curves were screened to exclude those with physically unreasonable values (supporting information Figure S1).

Seven hundred and fifty-two dispersion curves were used for the phase-velocity inversion on a grid of nodes spaced at 0.2° . The finite-frequency sensitivity kernels were calculated using the method of Yoshizawa and Kennett [2002] and the Pacific Ocean model by Nishimura and Forsyth [1989] (henceforth the NF89 model) for 0–4 Myr lithospheric age as the starting model. The tomographic inversion inverts for both isotropic and azimuthally anisotropic components of the Rayleigh wave phase velocity. However, robust results of anisotropy can be only resolved in a small region where most OBSs were concentrated, as previously discussed by Menke *et al.* [2015] which also included an S -wave splitting analysis of the OBS data. Therefore, the anisotropic components of the ANT results are not included in the rest of data processing and discussions. Since high signal-to-noise OBS ANT data are restricted in a narrow frequency band, we were only able to get robust phase velocities at periods from 8 to 18 s. Readers are referred to Zha *et al.* [2014] for technical details.

2.3. Phase-Velocity Inversion: Two-Plane Wave Method for Teleseismic Data

Following Wei *et al.* [2015], we selected seismograms of 357 earthquakes with surface-wave magnitudes (M_s) larger than 4.5 and epicentral distances between 30° and 150° , which occurred during the time when stations were operating (Figure 1d). Prior to the tomographic inversion, data were down-sampled to 1 sps and instrument responses were removed. For each period of interest from 19 to 88 s, we used a narrow bandpass filter (fourth-order Butterworth, zero-phase shift) centered at the frequency of interest to filter the seismograms. The filtered data were then windowed manually to isolate the fundamental mode of the Rayleigh wave. Noise in seismograms at long periods (>50 s) due to ocean swell and associated water pressure variations, as well as tilt caused by local currents, were removed by correcting the vertical channel using the horizontal and pressure channels [Webb and Crawford, 1999; Crawford and Webb, 2000; Bell *et al.*, 2015].

We then applied the two-plane-wave analysis method [Forsyth and Li, 2005] with 2-D Fréchet kernels [Yang and Forsyth, 2006] to invert for phase velocity at each period for both isotropic and anisotropic components. The advantages of this method include (1) addressing wavefront effects of global heterogeneities outside

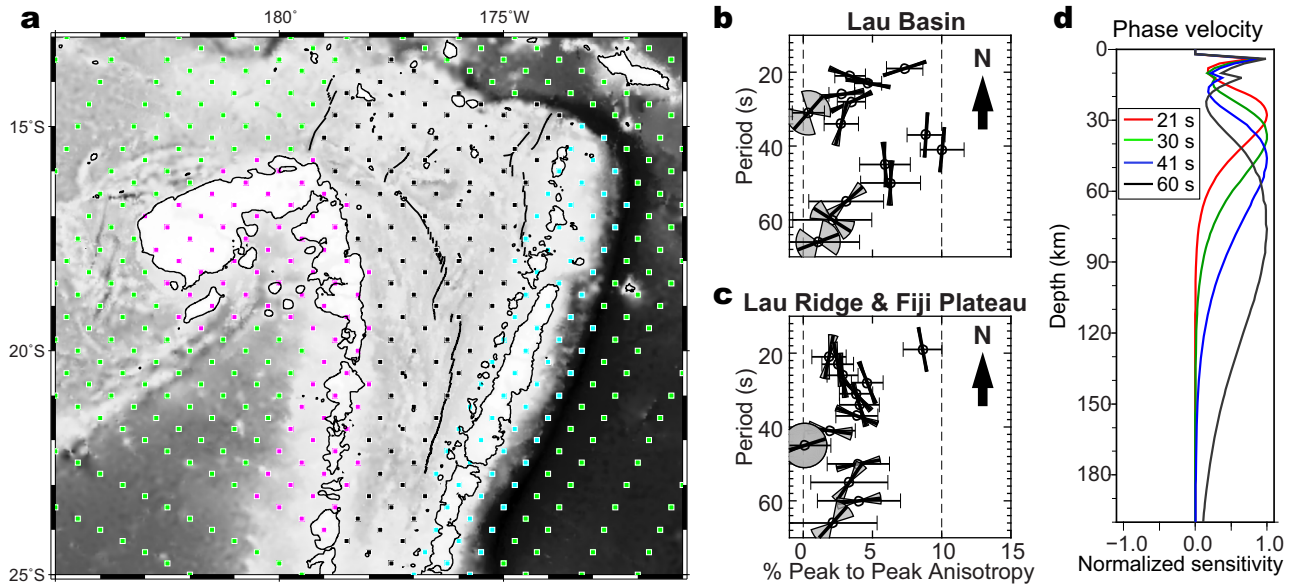


Figure 2. Azimuthal anisotropy determined by two-plane-wave tomography. (a) The TPWT nodes are divided into four tectonic subregions: the Lau Basin (black dots), the Fiji Plateau-Lau Ridge (magenta dots), the Tonga Ridge (cyan dots), and the surrounding region (green dots). Spreading centers and bathymetry contours are labeled as the same as Figure 1b. (b) Azimuthal anisotropy as a function of Rayleigh wave period for the Lau Basin. The period is displayed on the y axis with period increasing downward, since Rayleigh waves at shorter periods are sensitive to shallower structure. Short bars through each symbol show the fast direction in map view (the arrow shows the direction of north in map view). Error bars display doubled standard deviations. Errors of fast directions are shown as gray circular sectors. (c) Anisotropy for the Fiji Plateau-Lau Ridge, with symbols the same as in Figure 2b. (d) Phase velocity sensitivity kernels at example periods, calculated based on the average velocity model in Figure 4g.

of the study region with the two-plane-wave approximation, (2) correcting the effects of scattering and multipathing within the inversion region with the 2-D finite-frequency Fréchet kernels, (3) high computational efficiency, and (4) being able to combine two data sets over different time periods (1994 and 2009–2010) to expand the resolving region.

Seismic azimuthal anisotropy (only 2θ terms) was determined simultaneously with the isotropic phase velocities by the TPWT method. The data are not sufficient to determine the two-dimensional pattern of azimuthal anisotropy at each period, but they do provide constraints on the anisotropy of larger regions within the model. Therefore, we divided the study region into four tectonic subregions: the Lau Basin, the Fiji Plateau-Lau Ridge, the Tonga Ridge, and another region consisting of all the surrounding areas. We solved for the average anisotropy of each subregion as part of the TPWT inversion (Figure 2a). We then conducted a series of TPWT phase-velocity inversions with progressively finer grids (extending down to 58.7 km spacing) and smaller smoothing length (ending at 50–80 km depending on the period). Such a strategy can largely eliminate the dependence on the starting model and the *a priori* information [Rau and Forsyth, 2011]. More details of the TPWT phase-velocity inversions are discussed by Wei *et al.* [2015]. Both azimuthally isotropic and anisotropic components of the phase velocity were solved for simultaneously, but only the isotropic phase velocities were used for the SV-velocity inversion.

2.4. Combining Ambient Noise and Teleseismic Dispersion Curves

Combining the ANT and TPWT results provides more complete measurements of phase velocity for the next step of the SV-velocity inversion. However, as these two methods are based on different principles and assumptions, the results of phase velocity at the common periods from two methods are usually not identical [Yao *et al.*, 2006]. In this study, we were not able to resolve the results of ANT and TPWT at a common period because of the high noise level of the OBS data. The data around 20 s period had too much seafloor noise from other sources to obtain good results with ANT, and 20 s is approximately the shortest period for realistic application of TPWT. Figure 3 shows that the resulting phase velocities agree well at the adjacent periods, although small-scale discrepancies still exist. We thus conclude that the real phase-velocity uncertainties are larger than the standard deviations given by the ANT and TPWT inversions because of the systematic errors introduced by inversion theories and assumptions.

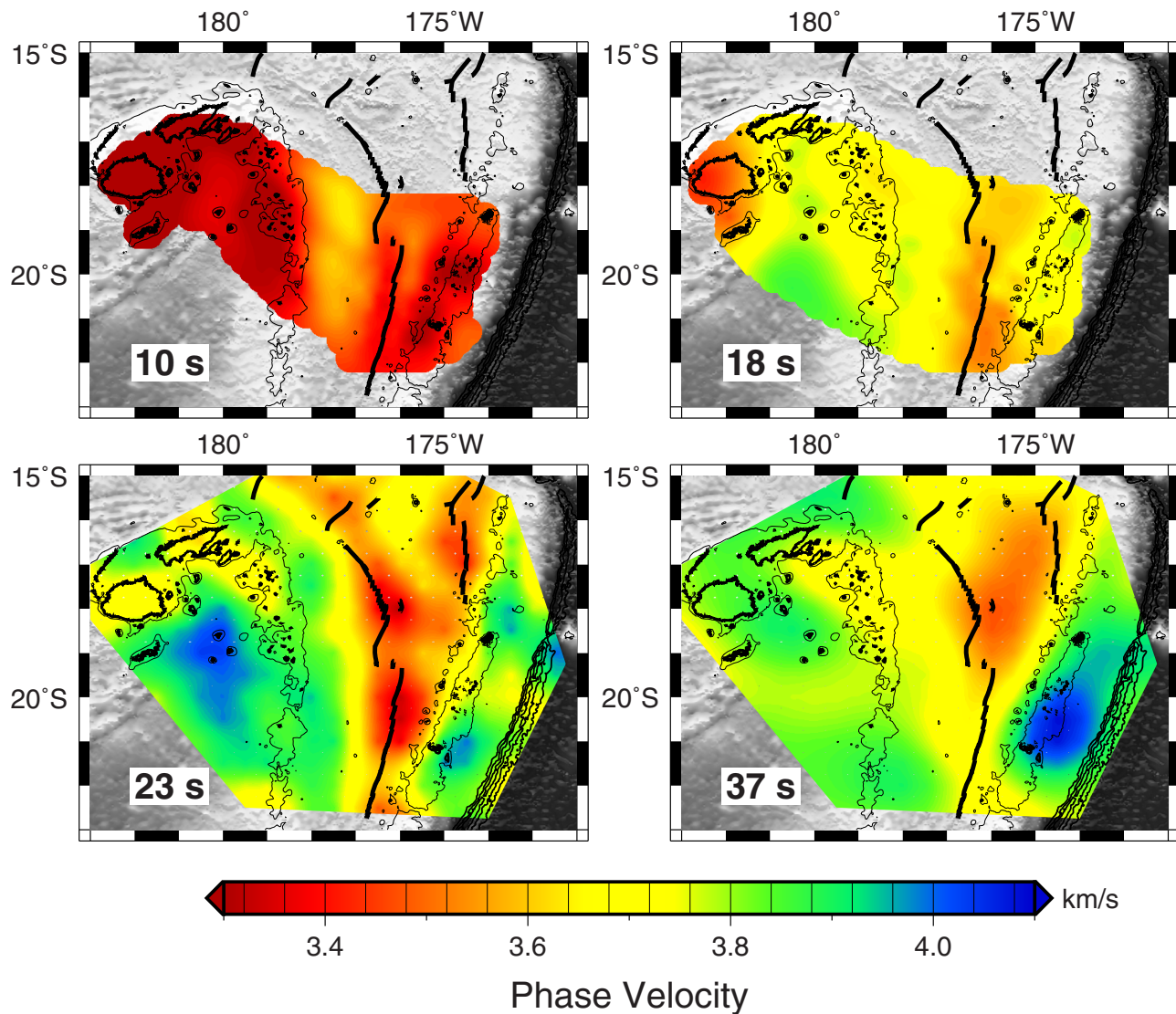


Figure 3. Maps of azimuthally averaged phase velocity at periods of 10 and 18 s inverted by ANT, 23 and 37 s inverted by TPWT. Azimuthal anisotropy is inverted simultaneously, but is excluded in the next step of SV-velocity inversion. Spreading centers are denoted by black curves. The 1 km bathymetric contour and the coastlines are shown to outline the Tonga Ridge, Tofua arc, Lau Ridge, and Fiji Plateau. The 7, 8, 9, and 10 km water depth contours are also shown to delineate the Tonga Trench.

The two sets of dispersion curves were combined in the geographical region well resolved by both methods (blue outline in Figure 1c) for the SV-velocity inversion. The phase velocities were interpolated onto a uniform grid of nodes with spaced at 0.2° before being combined at each node (Figure 1c). The phase velocities at periods of 19 and 21 s were discarded due to the large uncertainties. The uncertainties at other periods were normalized at each period that the standard deviation of the best-resolved node becomes equal to a reference value given below. According to previous experience [Yang *et al.*, 2008; Shen *et al.*, 2013], the reference uncertainty is assigned as 0.2 km/s for periods of 18–23 s, 0.15 km/s for periods of 16, 17, 25.6, and 28.2 s, and 0.1 km/s for other periods. A modified running average filter was applied so that the resulting dispersion curve is smoother but the phase velocity at each period can be adjusted only within the uncertainties. In the outer regions where no ANT results were available, we used phase velocities from the TPWT at all periods to invert for SV-velocity (Figure 4c), so the shallow structures have lower resolution in these areas. The edge of the region with adequate resolution (gray polygon in Figure 1c) was defined based on resolution tests as Wei *et al.* [2015].

It is worthwhile to examine the noticeable depression of the dispersion curve in the period range of 15–35 s at certain nodes. This depression can be observed solely by TPWT (Figure 4c) or by combining ANT and

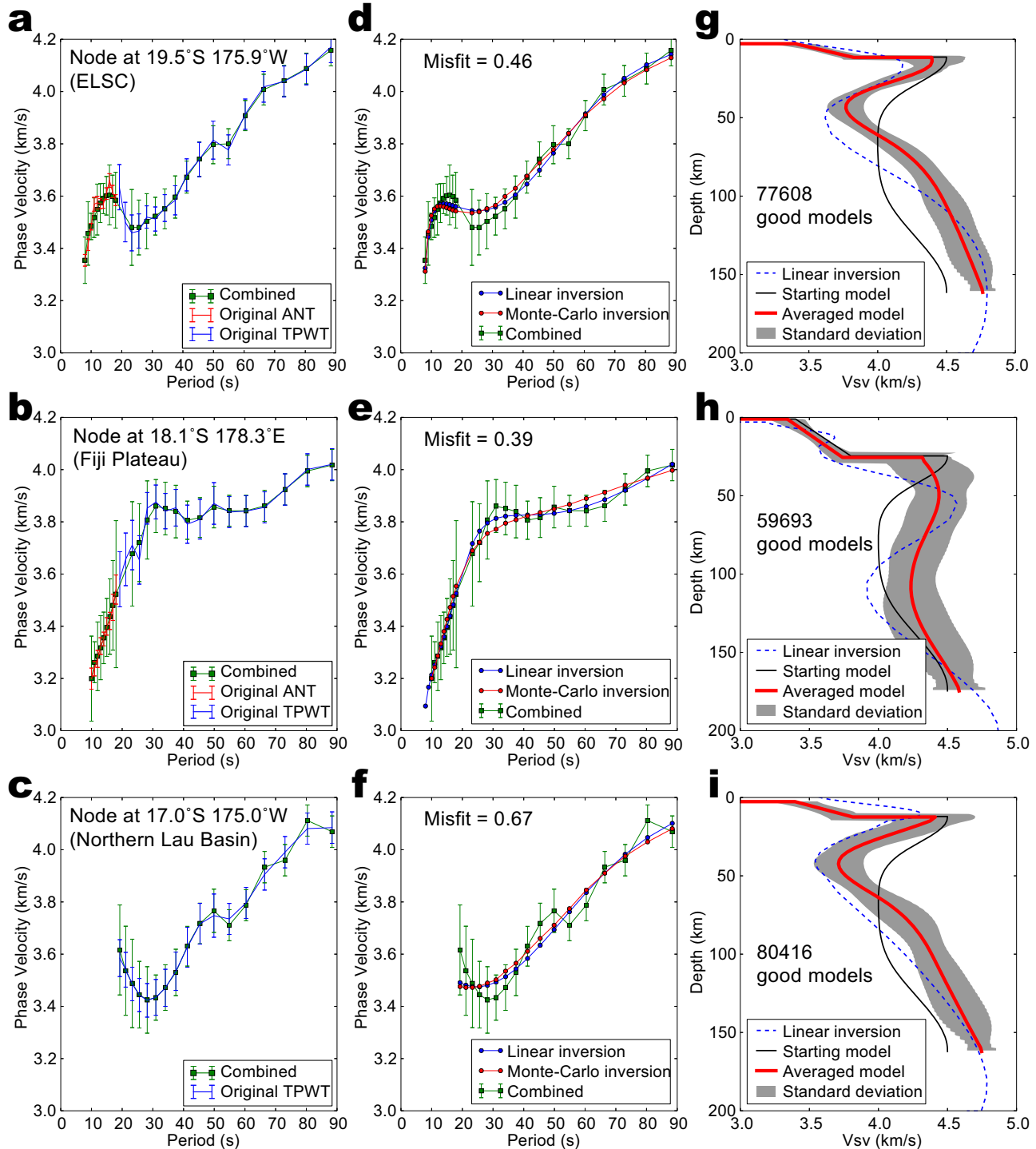


Figure 4. Examples of the joint dispersion curve and the results of the SV-velocity inversion. Each row shows the dispersion curves and SV-velocity models of nodes at the ELSC (a, d, g), at the Fiji Plateau (b, e, h), and in the northern Lau Basin without ANT coverage (c, f, i). Their locations are shown as magenta stars in Figure 1c. (a–c) Original dispersion curves measured by the ANT (red) and the TPWT (blue) with error bars showing doubled standard deviations. Green curves indicate the combined dispersion curve with amplified uncertainties. (d–f) Fit to the observed dispersion curves (green) with dispersion curves corresponding to the linearized inversion (blue), and the average SV-velocity model from the Monte-Carlo inversion (red). The misfit is defined as the square root of the reduced χ^2 misfit of the average model from the Monte-Carlo inversion. (g–i) The average of accepted SV-wave velocity models (red) with the standard deviations (gray shade) are compared with the starting model (black) and the linearized inversion result (blue dashed curve).

TPWT results (Figure 4a), and has been previously observed at the East Pacific Rise [Forsyth *et al.*, 1998]. Therefore, we conclude that the depression of the dispersion curve convincingly reflects a strong low-velocity zone (LVZ) beneath a very thin lithosphere.

2.5. SV-Wave-Velocity Inversion With a Bayesian Monte-Carlo Algorithm

Previous studies [e.g., *Wei et al.*, 2015] suggest that the linearized inversion of SV-wave velocity from phase velocity dispersion curves [*Herrmann*, 2004] depends upon the starting model. In order to avoid the potential biases due to the starting model, and to better apply *a priori* constraints in a systematic way, we use a Bayesian Monte-Carlo method [*Shen et al.*, 2012] to invert for the azimuthally averaged SV-wave velocity at each node. Ideally we could invert the azimuthally varying phase velocities for shear anisotropy as a function of depth [e.g., *Montagner and Nataf*, 1986], but given the limited lateral resolution of azimuthal anisotropy and the large number of unknowns involved in the inversion, we instead provide a qualitative interpretation of the anisotropy.

The Bayesian Monte-Carlo method constructs a prior distribution of SV velocity models at each node, which is defined by perturbations relative to the starting model and model constraints. The posterior distribution thus provides statistical information of all possible SV-velocity models that satisfy the Rayleigh wave dispersion data within tolerances depending on data uncertainties. Each model consists four layers on top of a half-space: (1) water with a fixed thickness from bathymetry in Lindquist et al. [2004] (Figure 1b), (2) sediments, (3) crust, and (4) upper mantle from the Moho to 150 depth. The sedimentary layer is described by two parameters: a layer thickness of 0.5 km with an allowed perturbation of ± 0.5 km and a constant V_{SV} of 2 km/s with a permitted perturbation of ± 1 km/s. The crust is assumed to have a linear velocity gradient with depth, and is described by three parameters: a layer thickness and V_{SV} at the top and bottom of the layer. The crustal thickness, varying from 7 to 25 km, and its perturbation are designed based on a previous seismic refraction survey [*Crawford et al.*, 2003] and preliminary results of a receiver function analysis using the land-station data [*Chen et al.*, 2015] (supporting information Figures S2a and S2b). The top and bottom crustal V_{SV} are set as 3.4 and 3.8 km/s, respectively, with a perturbation of ± 0.3 km/s. The upper mantle V_{SV} is parameterized by a B-spline, which is defined by 7 nodes with a perturbation of $\pm 30\%$ for each of the first 5 nodes and 20% for the last 2 nodes. We also applied a physical dispersion correction with a reference period of 1 s [*Kanamori and Anderson*, 1977] using a 1-D Q model simplified from a seismic attenuation study in the same region [*Wei*, 2016]. Compared to the PREM, our 1-D Q model has a high-attenuation layer in the uppermost mantle: $Q_5 = 30$ at 0–50 km depth. This is appropriate for the nodes in the Lau Basin, but would slightly underestimate the shallow velocities beneath the Fiji Plateau-Lau Ridge. The Monte-Carlo inversion determines both an average of all the models providing a statistically acceptable fit to the data, and the specific model with the best fit to the data. In this study, we follow the procedure of previous applications [e.g., *Shen et al.*, 2012] and use the average model for plotting and interpreting the results.

Examples of the SV-velocity inversion at three representative nodes are shown in Figure 4. The results of the Bayesian Monte-Carlo inversion fit the measured dispersion curves as well as the linearized inversion. But this technique significantly reduces the dependence of the result on the starting model and damps the artificial oscillations that are not required by the data (Figure 4h). Additionally, the Monte-Carlo inversion can fully utilize the uncertainties of phase velocity and is able to estimate errors of SV-velocity.

3. Results

3.1. Phase Velocity

Figure 3 shows 2-D maps of azimuthally averaged phase velocities at representative periods from ANT and TPWT. Since the ANT inverts Green's functions for propagation between station pairs, the well resolved region is confined to a smaller area. The TPWT provides results encompassing larger areas, because it has some limited resolution outside the array and because we included data from the 1994 deployments. Due to the varying wavelengths of Rayleigh waves, the resolution length of the ANT is as small as 50 km at the shortest periods, whereas the TPWT has larger resolving lengths (supporting information Figure S3b). It is intriguing whether the absence of the low-velocity anomalies beneath the VFR at long periods is due to lack of resolution as the V-shaped low-velocity zone (LVZ) narrows to the south. However, a resolution test using an input model with a V-shaped LVZ shows that the low-velocity anomalies at the VFR should be recovered as well as that in the north. As discussed in section 2.4, the L_2 norm of the model underestimates the phase-velocity uncertainties. We thus amplify the uncertainties according to previous experience (Figures 4a–4c).

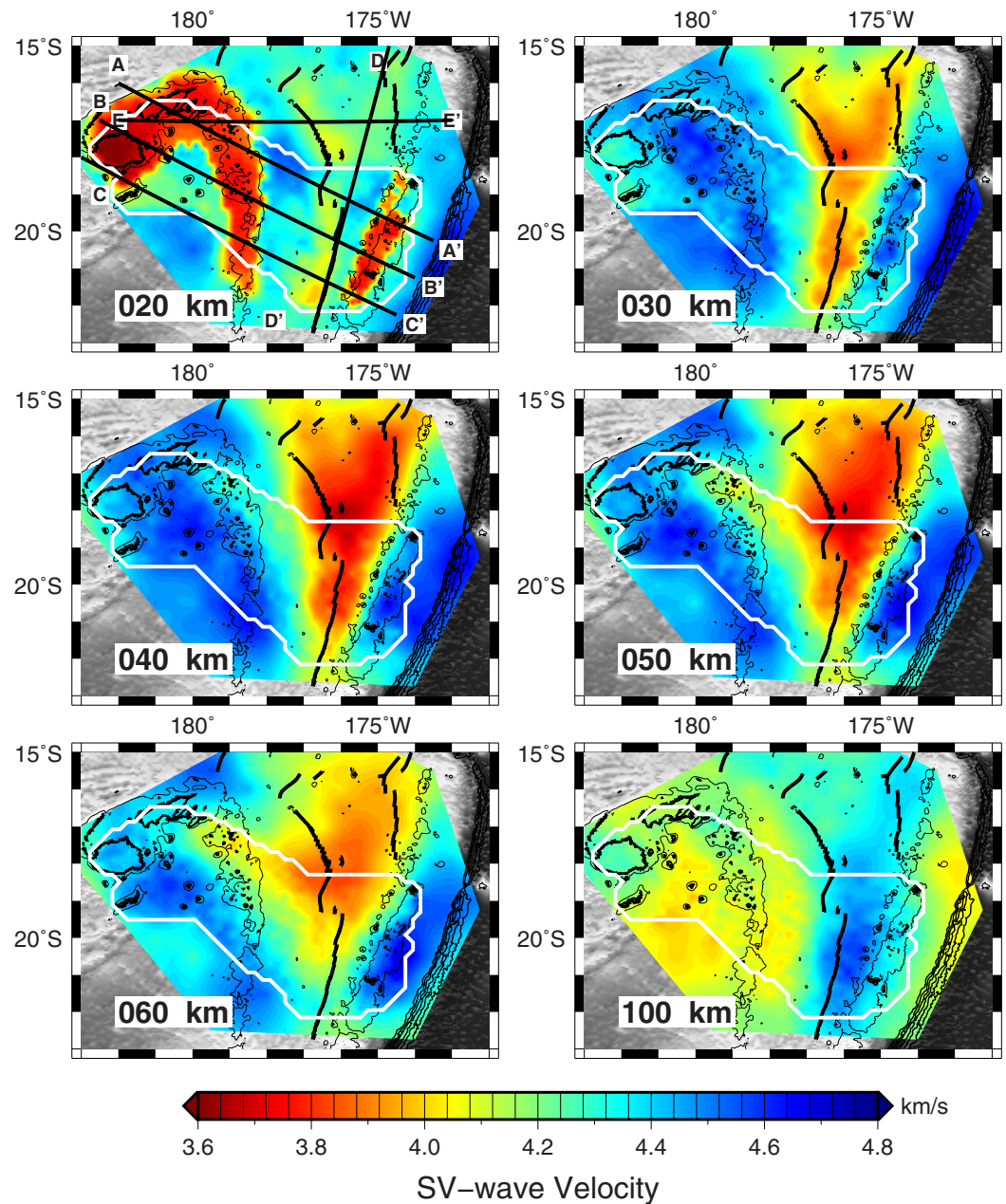


Figure 5. Maps of azimuthally averaged SV-velocity at 20, 30, 40, 50, 60, and 100 km depths relative to the sea level. White contour encloses the region of the ANT-TWPT joint inversion. Black straight lines show the cross sections in Figure 6. The cross sections A-A', B-B', and C-C' start from and extend perpendicular to the Tonga Trench. Spreading centers and bathymetry contours are labeled as in Figure 3.

Azimuthal seismic anisotropy is determined simultaneously with the isotropic phase velocities by the TPWT data, with the results shown in Figure 2. This analysis provides good resolution of the azimuthal anisotropy in regions with similar dimensions in each direction but has limited usefulness for elongated ones. As the anisotropy is poorly resolved in the narrow Tonga Ridge region, we thus only interpret the results for the Lau Basin and the Fiji Plateau-Lau Ridge (Figures 2b and 2c). The magnitude of anisotropy varies depending upon the chosen parameters of the tomographic inversion such as smoothing length and damping coefficient, but the fast directions are robust. We thus confine our interpretation to the directions of anisotropy.

3.2. Azimuthally Averaged SV-Velocity

The azimuthally averaged SV-velocity structure of the Tonga-Lau-Fiji region from the average model of the Monte-Carlo inversion at each node is shown in Figures 5 and 6. The model fits to the data are good, such that the square

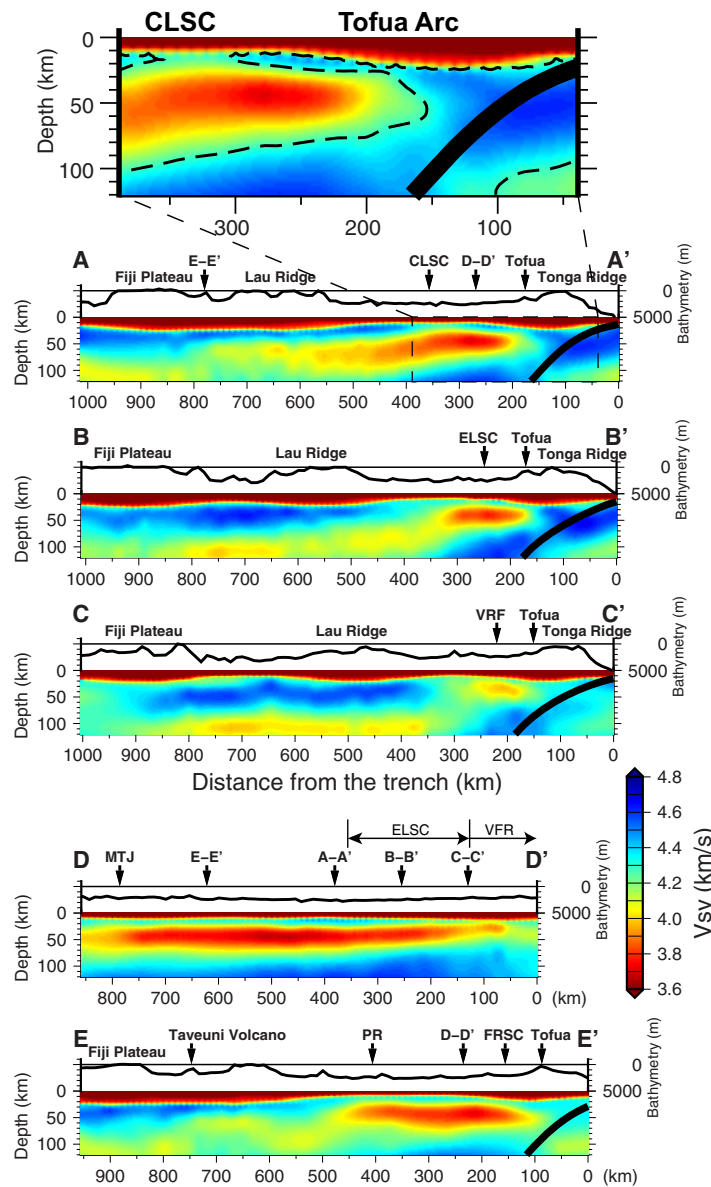


Figure 6. Cross sections of azimuthally averaged SV-velocity. Black bold curves delineate the surface of the subducting slab from the Slab 1.0 model [Hayes et al., 2012]. The bathymetry is plotted on top with vertical exaggeration. The Lau Basin part of the cross section A-A' is enlarged with a contour of 4.28 km/s to highlight the interactions between arc and back-arc.

The most obvious feature in our results is the contrast between the Lau Basin and the remnant arcs. The Tonga Ridge, Fiji Plateau, and Lau Ridge are characterized by low velocities at depths shallower than 25 km and by high velocities at 25–50 km depths, indicating the crust and mantle lithosphere, respectively. In contrast, a V-shaped LVZ is imaged in the uppermost mantle of the Lau Basin, forming an asymmetric triangular region beneath the back-arc spreading PR centers. As discussed in section 3.1, the V-shape LVZ is well resolved (supporting information Figure S3b), and thus we are confident to conclude that the strength of low-velocity anomalies at 40–50 km depth decreases from north to south along the spreading centers. The low-velocity anomalies appear somewhat less extreme compared to the results in Wei et al. [2015], due to the additional ambient-noise constraints and the Monte-Carlo method. Low velocities beneath the spreading centers are no longer observed at depths of about 100 km, leaving high velocities representing the subducting slab in the eastern area and low velocities in the western back-arc as the dominant structures.

root of the reduced χ^2 misfit of the average model from the Bayesian Monte-Carlo inversion at each node is consistently less than 1 (supporting information Figure S4). The resulting crustal thickness changes little compared to the starting models (supporting information Figure S2), and the changes are much smaller than the allowed perturbation. This reflects that our data are not able to resolve the Moho depth precisely without constraints from converted seismic waves (e.g., receiver functions), but also suggests that the starting models fit the data reasonably well.

Thanks to the high resolution of the ANT phase velocity maps at short periods, small-scale features are well resolved at shallow depths within the region of the ANT-TPWT joint inversion. But this resolution contrast also introduces some artificial discontinuous features at the boundary of the joint-inversion region. For instance, low-velocity anomalies are imaged at 20 km depth beneath the Lau Extensional Transform Zone (LETZ) in Figure 5, but stop in an artificial way at the northern boundary of the joint-inversion region (white contour) instead of extending southward to the CLSC. The shallow velocities within the white contour inverting both ambient-noise and teleseismic data are better constrained, and we hesitate to interpret any of the shallow features along this boundary.

4. Discussions

4.1. Factors Controlling Seismic Velocity

Interpreting seismic observations in terms of material properties and processes is nonunique since many factors can influence seismic velocity. A primary objective of this study is to investigate the melting process in the arc and back-arc, but in order to study the distribution of melt, it is necessary to distinguish the effects of melt from other effects. Generally speaking, seismic properties of mantle rocks are controlled by temperature, composition, grain size, and melt/free fluid through anharmonic and anelastic behaviors [e.g., *Wiens et al.*, 2008; *Abers et al.*, 2014].

Thermal variations affect seismic properties in both anharmonic and anelastic ways. For high-frequency waves, a reduction in density due to thermal expansion (anharmonic oscillation) results in decreases in elastic moduli and thus seismic velocity [*Anderson*, 2007]. Additionally in the seismically observable frequency band (0.01–1 Hz), anelasticity can be equivalently important as seismic attenuation also affects seismic velocity [*Karato*, 1993]. The effects of temperature on anharmonic behavior can be determined by ultrasonic experiments [e.g., *Isaak*, 1992], but study of anelastic behavior requires rock deformation experiments at seismic frequencies [e.g., *Faul and Jackson*, 2005; *Jackson and Faul*, 2010; *McCarthy et al.*, 2011]. Although it is difficult to quantify the thermal effects on seismic velocity, seismological and geochemical comparisons among different back-arc basins suggest that temperature plays a dominant role in the back-arc system [*Wiens et al.*, 2006].

Compositional variations of mantle rocks have been considered unimportant to the variations observed in seismic results because the shear modulus is increased by the depletion of FeO in olivine but also reduced by the depletion of Al₂O₃ [*Faul and Jackson*, 2005]. Studies on natural peridotite [*Lee*, 2003; *Schutt and Leshner*, 2010] indicate that melt depletion leads to an increase of about 2–3% in *S*-wave velocity, much smaller than regional velocity variations (>10%) observed in our results.

Water (hydrogen) dissolved in nominally anhydrous minerals is thought to reduce seismic velocity by increasing anelasticity [*Karato*, 2003]. However, since water also enhances grain growth which has an opposite effect on anelasticity, this competing effect may eliminate the effects of water on seismic properties [*Abers et al.*, 2014]. In contrast to the relatively dry MORBs with water concentrations of 0.01–0.05 wt % in the mantle source, the CLSC and ELSC lie on the upper bound of the MORB regime with a water content of 0.04–0.06 wt %, and the VFR is characterized with a significantly larger water content of 0.22 wt % [*Kelley et al.*, 2006]. Since the water concentrations in many regions beneath the Lau Basin exceed the maximum storage capacity of nominally anhydrous mantle minerals [*Kelley et al.*, 2006], water will be present in the mantle wedge. It is likely to be in the form of an aqueous melt, given the high temperatures present in the back-arc upper mantle [*Hirschmann et al.*, 2005]. Along the Lau spreading centers, the magnitude of low-velocity anomaly increases from south to north (Figure 5), opposite to the trend of decreasing water content [*Kelley et al.*, 2006]. This implies that the water content is not the predominant factor controlling the seismic velocity. The mantle water content is also higher near the slab, whereas the largest seismic anomalies occur beneath the back-arc spreading center, again suggesting that the observed low-velocity anomalies do not result directly from mantle water.

Melt introduces more complex effects on seismic velocity. It is generally accepted that partial melt decreases the anharmonic shear modulus of rocks through a poroelastic effect and the reduction of *S*-wave velocity highly depends on melt geometry [e.g., *Hammond and Humphreys*, 2000a; *Takei*, 2002]. However, the effects of partial melt on seismic attenuation and consequently seismic velocity through anelastic behavior have not been well constrained. *Hammond and Humphreys* [2000b] predicted very little melt-related attenuation in the seismic frequency band in numerical calculations. In contrast, *Faul et al.* [2004] found that melt influences seismic attenuation based on rock deformation experiments through grain-boundary sliding or melt squirt mechanism [*Faul and Jackson*, 2015]. More recent experiments on analogous borneol-diphenylamine aggregates [*McCarthy and Takei*, 2011] and fine-grained peridotite [*Sundberg and Cooper*, 2010] also suggest melt-related seismic velocity reduction. On the other hand, partial melting may dehydrate residual mantle rocks [*Hirth and Kohlstedt*, 1996], causing a decrease in seismic attenuation and an increase in seismic velocity due to a reduction in anelasticity if the melt is largely extracted. The latter effect also depends upon the water supply. Geochemical studies reveal a positive correlation between the mantle water concentration and the extent of melting beneath the back-arc spreading centers [*Kelley et al.*, 2006], in contrast to a

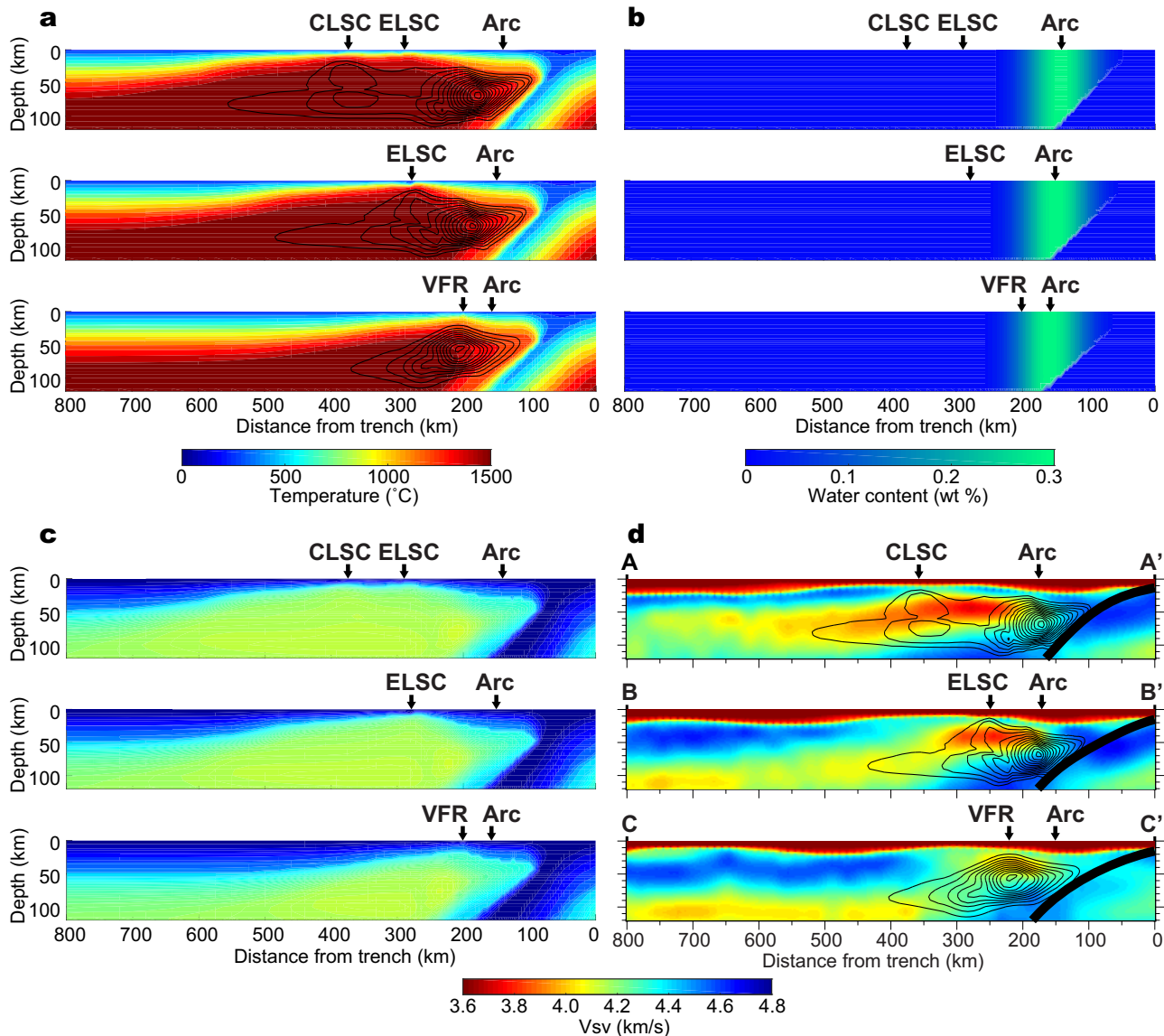


Figure 7. Cross sections of temperature and mantle water structure from the geodynamical model and the predicted SV-wave velocities. (a) Numerical models of temperature with a potential temperature of 1450°C. Black contours show the local melt production in 1% increments. (b) Water distribution with a background value of 0.01 wt % superposed by a hydrous region beneath the arc. The hydrous region is centered beneath the arc with a Gaussian-shaped horizontal section ranging from 0.01 to 0.3 wt %. (c) Predicted SV-velocities based on numerical models in (a) and (b), extended Burgers model fit of experimental results relating temperature and velocity [Jackson and Faul, 2010], and the effects of water extrapolated from rheological relationships [Karato, 2012]. Further details of the conversion are given in the text. (d) Cross sections A-A', B-B', and C-C' from Figure 6, which are located similarly to the cross sections in (c). Contours of melt production from (a) are superposed with slight stretching to accommodate the arc and back-arc locations. The seismic LVZ does not necessarily correspond with the melt production contours as the former reflects the melt content remaining in the mantle. Notice the SV-velocity color scales in (c) and (d) are the same.

negative correlation beneath the MORs [Asimow and Langmuir, 2003]. So even the mantle water content beneath the CLSC lies in the MORB regime close to the upper limit, the water supply beneath most Lau back-arc spreading centers should be large enough that the effects of mantle dehydration due to melting can be neglected. Therefore, melt should significantly reduce seismic velocity beneath the back-arc where an abundance of melts are expected, whereas free water, if exists, could reduce seismic velocity near the slab.

Following Wei *et al.* [2015], we explore the expected effects of temperature and water content on Lau Basin SV-wave velocities using new 2-D numerical models of mantle wedge flow (Figure 7). The thermal models were produced in the same way as that in Conder *et al.* [2002] and Wiens *et al.* [2008], except with the additions of a background water content of 0.01 wt % and a hydrous region near the slab (Figure 7a). The

hydrous region is centered beneath the approximate arc location, and is expressed as a vertical arc-parallel Gaussian-shaped region with a water content ranging from 0 to 0.3 wt % (Figure 7b). To model decompression melting beneath the arc and back-arc (black contours in Figure 7a), we followed *Conder et al.* [2002] to calculate the decompression melt production rate of a parcel of mantle based on temperature, depth, previous melting history, and upwelling rate, assuming a normal MORB source starting mantle composition with the water content shown in Figure 7b. The conversion to *S*-wave velocity is based on available rock physical models and experimental constraints, including an extended Burgers model that fits data of forced torsional oscillation experiments [*Jackson and Faul*, 2010] and the effects of water as proposed by *Karato* [2012]. The calculated isotropic *S*-wave velocities are converted to *SV*-wave velocities using the radial anisotropy as a function of depth from the NF89 0–4 Myr model [*Nishimura and Forsyth*, 1989]. Since the potential temperature used in the numerical models is 1450°C, which is consistent with the value revealed at the CLSC but slightly higher than that at the ELSC and VFR [*Wei et al.*, 2015], and we assume the largest possible water effects ($r = 2$ in *Karato* [2012] model), the predicted values in Figure 7 should provide a lower bound for *SV*-wave velocity. We acknowledge that several parameters of the models are poorly constrained, but neither using other reasonable parameters nor alternative conversion methods such as *Goes et al.* [2012] allows us to explain the low velocities solely by variations of temperature and water content. Therefore, it is reasonable to attribute the extremely low *SV*-wave velocities at about 30–70 km depth to partial melt, even though quantitatively determining the mantle porosity filled with melt (melt porosity hereafter) from seismic velocities is beyond the current knowledge of rock physics.

In summary, the large-scale contrast of the subducting slab with fast seismic velocities versus much of the rest of the modeled region is interpreted as being mostly thermally controlled. Basaltic melt with variable water content, which significantly decreases seismic velocity in the melting region, provides a good explanation for the very low-velocity anomalies observed in the Lau Basin beneath the spreading centers and volcanic arc.

4.2. CLSC-ELSC-VFR, Tofua Arc, and Tonga Ridge

At shallow depths (20 km in Figure 5), the low-velocity anomalies correlate well with topography, showing the contrast between the thicker arc crust and the thin oceanic crust. The back-arc low-velocity anomalies at 20 km depth indicate hot asthenosphere and perhaps partial melt in the back-arc uppermost mantle.

At greater depths, an LVZ encompasses an N-S striking broad region beneath the Lau Basin. Since these depths are convincingly below the lithosphere-asthenosphere boundary predicted by a simple half-space cooling model [*Wei et al.*, 2015], this *V*-shaped LVZ illustrates a contrast between the hot asthenosphere of the Lau Basin and the cold and thick lithosphere of the Tonga and Lau Ridges. Cross sections (Figure 6) show this LVZ becoming deeper with distance away from the arc, indicative of a broad and asymmetric hot region beneath the back-arc basin. As discussed in the previous sections, the widespread low velocity in the mantle indicates high temperature, while the extremely low-velocity anomalies at 30–70 km depths beneath the arc and spreading centers represent high melt porosity in the mantle wedge. The inclined LVZ indicates that hot mantle upwells from the deep west governed by the wedge corner flow [*Conder et al.*, 2002], triggers extensive passive decompression melting, similar to the asymmetric melting region observed beneath the East Pacific Rise (EPR) [*Forsyth et al.*, 1998; *The MELT Seismic Team*, 1998]. The onset of melt, as defined by very large amplitude low-velocity anomalies, appears to occur at 70–80 km depths west of the spreading centers (Figure 6), consistent with petrological expectations [*Shen and Forsyth*, 1995]. The off-axis melt may percolate toward to spreading centers along the bottom of the thermal/compositional lithosphere driven by the focusing effects [*Sparks and Parmentier*, 1993; *Phipps Morgan*, 1997]. Off-ridge volcanism in the western Lau Basin [*Falloon et al.*, 1992] may also be related to these melts.

The *V*-shaped LVZ can be explained by the opening of the back-arc basin, since the hot asthenosphere is wider in the north than in the south at a certain depth. However, this mechanism cannot explain the N-S striking variations of the extremely low-velocity anomalies along the spreading centers, as the along-strike thermal variation determined by geochemical thermobarometry [*Lee et al.*, 2009] is only about 50°C, potentially resulting in a slight change in velocity of 0.1 km/s [*Wei et al.*, 2015]. Therefore, we attribute these along-strike variations to changes in melt porosity. Our results suggest the melt porosity is highest beneath the northeastern Lau Basin and the CLSC, and decreases southward to the VFR. Additionally, the melting commences deeper in the north, and becomes shallower in the south. In contrast, higher melt production

and deeper onset of melting are expected in the south due to the higher mantle water content there according to previous numerical models [Harmon and Blackman, 2010], petrological studies [Kelley et al., 2006], and surveys of crustal structure [Dunn and Martinez, 2011].

Wei et al. [2015] interpreted these discrepancies as consequences of the varying efficiency of melt extraction, which is influenced by the water released from the slab or the existence of a nearby spreading center. If we assume the melt transport to be an equilibrium porous flow, it should follow Darcy's law with $q \propto d^2 \phi^n / \mu$, where q is the melt flux, d is the grain size, ϕ is the porosity, μ is the melt viscosity, and n is about 2.6 [Miller et al., 2014]. At the VFR, a large amount of water from the slab enters the back-arc melting region, which reduces melt viscosity and/or increases mantle grain size. Both the reduction of melt viscosity and the increase in grain size will increase the mobility of the melt through the matrix and enhance the upward melt transport. At the CLSC, the mantle water content drops to the MORB regime [Kelley et al., 2006], so water has little effect on melt extraction. The large melt production helps the mantle to retain the partial melt. In the northeastern Lau Basin, between the CLSC and the FRSC, melts generated in the mantle wedge are trapped in the mantle because of the lack of an effective magma channel, and either slowly solidify or migrate laterally large distances to one of the spreading centers. This gives rise to the large velocity anomalies found at 40–50 km depth in this region even though there is no active spreading center nearby.

The combination of ANT and TPWT data greatly strengthens our capability of studying the interactions between the arc and back-arc melting. The arc is presumably dominated by flux melting whereas the back-arc is dominated by decompression melting. The cross section A-A' and the detailed inset (Figure 6) show that in the north where the CLSC is distant from the volcanic arc, the volcanic arc and the back-arc spreading center are separated by a region of ~ 20 km thick lithosphere. The large velocity anomaly (i.e., $V_s < 3.9$ km/s) does not extend all the way to the Moho, but rather stops at 30 km depth beneath the CLSC and about 40 km depth beneath the volcanic arc. These depths likely represent the top of the mantle melting regions, particularly in view of the final melt equilibrium depth of 35 km determined from geobarometry for the CLSC [Wei et al., 2015]. Despite the thickening of the lithosphere between the arc and the CLSC, the main melting region at depths of 40–70 km depth seems to be relatively continuous between the arc and the back-arc spreading center (Figure 6, A-A' and inset). It is interesting to compare these results to tomographic images across the Mariana arc and back-arc, where the arc and back-arc spreading center are separated by a similar distance. In Mariana, the mantle velocity anomaly is also deeper than the anomaly beneath the spreading center, but there is a much more pronounced gap in the main mantle melting region [Barklage et al., 2015].

In the south where the VFR is closer to the arc, two melting regions with different mechanisms interact at all depths. These observations provide the direct seismic evidence for the distance-controlling hypothesis that the interactions between the arc and back-arc melting predominantly determine the along-strike variations of geology, petrology, and geomorphology [Martinez and Taylor, 2002]. Due to the low lateral resolution of Rayleigh wave tomography, it is difficult to resolve the details of flux melting, especially the slab dehydration and the mantle wedge hydration. The low-velocity anomalies are generally weaker beneath the Tofua volcanic arc than in the back-arc. It could partially result from the strong depletion at the arc, but also imply that the melt porosity beneath the arc is significantly lower than that in the back-arc. The more water-rich arc magma segregates and erupts more efficiently compared to the back-arc magma that is partially retained in the mantle [Kelley et al., 2006].

Comparisons among cross sections also reveal the cause of the abrupt change in geochemical signatures and axial morphology along the ELSC-VFR at about 20.6°S and 21.2°S [Bézos et al., 2009; Escrig et al., 2009]. The cross sections B-B' and C-C' (Figure 6) suggest that the major sources of mantle materials at the CLSC and ELSC are the Australian mantle from the west with a small contribution from the slab-influenced mantle wedge. In contrast, the LVZ beneath the VFR appears to be disconnected to the west (cross section C-C' in Figure 6), suggesting that the supply of mantle material from the Australian asthenosphere is impeded by the thick lithosphere of the Lau Ridge. On the other hand, the influence of subduction increases consistently to become the dominant material source at the VFR. We propose that the sudden transition in magma chemistry at about 20.6°S and 21.2°S represents the transition between spreading centers fed by Australian mantle from the west and those restricted to melts generated near the Tonga slab. In other words, this abrupt transition not only reflects a gradual change in the influence from subduction, but also another gradual change in the influence from the Australian mantle in an opposite trend. We also notice that these

variations of seismic velocity structure coincide with a transition in the extinct Lau Ridge between uplifted section to the north and the submerged section to the south. Our inferences suggest that the uplifted section to the north corresponds to areas underlain by rising warm mantle capable of providing buoyancy, and the southern section lacking such mantle structure.

4.3. Fiji Plateau and Lau Ridge

High-velocity anomalies in the uppermost mantle of the Fiji Plateau-Lau Ridge indicate that these ancient arc terrains are underlain by lithosphere with a thickness of 60–80 km (Figures 5 and 6). The asthenosphere is characterized by an LVZ with SV -velocity of 4.0–4.2 km/s, similar to the typical SV -velocity for young oceanic asthenosphere [Nishimura and Forsyth, 1989]. A comparison of these results with the velocity structure predicted by thermal models (Figure 7) shows that the low velocities in the LVZ can be explained by thermal variations without any significant melt content, although the role of small amounts of partial melt in the asthenosphere generally is a subject of considerable debate [e.g., Goes *et al.*, 2012; Holtzman, 2016].

One intriguing feature is a low-velocity anomaly at 50–60 km depth beneath the active Taveuni Volcano and the northernmost Lau islands, which connects to the broad V-shaped LVZ in the central Lau Basin (Figure 5). Thus the lithosphere of the eastern Fiji Plateau and the northern Lau Ridge is only about 50 km thick compared to ~80 km in surrounding areas, suggesting lithospheric material was removed or never existed at depths below 50 km. This feature cannot be an artifact due to resolution changes along the ANT-TPWT joint-inversion region boundary, because it is much deeper than the depth corresponding to the longest ANT period and is clearly shown in the TPWT phase velocity map at 37 s period (Figure 3). Although this low-velocity anomaly appears to be an arm extending from the V-shaped LVZ beneath the Lau Basin, trace element analyses suggest that the magmatism in this region rejuvenated since 3 Ma with a strong ocean-island basalt (OIB) affinity [Gill and Whelan, 1989]. Isotopic studies reveal that these magmas have a similar origin with the Samoa mantle plume rather than the Lau spreading centers [Pearce *et al.*, 2007]. Lytle *et al.* [2012] suggest the existence of an additional mantle plume in the Fiji region to explain geochemical trends in the northwestern Lau Basin. Therefore, one reasonable explanation is that upwelling hot material from deep mantle, perhaps related to the Samoa mantle plume, heated and eroded the lithosphere beneath this region.

4.4. Northern Lau Basin

Although it is widely accepted that materials from the Samoan mantle plume enter into the Tonga mantle wedge from north [Turner and Hawkesworth, 1998; Pearce *et al.*, 2007], the details of this process, especially beneath the northern Lau Basin, are unclear. There are at least two systems of back-arc spreading centers in this region: the eastern series consisting of the Fonualei Rift and Spreading Center (FRSC) and the Mangatolu Triple Junction (MTJ) close to the Tonga Trench, and the western series including the LETZ, the Peggy Ridge (PR), and the Northwest Lau Spreading Center (NWLSC). Recent isotopic geochemical analyses of rock samples collected from these two series reveal heterogeneities across the northern Lau Basin. In the west along the NWLSC-PR-LETZ, the diversity of geochemical signatures led Lytle *et al.* [2012] to propose multiple magma origins from more than two mantle sources, including the Samoan mantle plume, a shallow MORB-like source beneath the spreading centers, and a possible second plume from deep west. However, Price *et al.* [2014] suggest that this geochemical diversity can be explained by the original single plume model mixed with ambient depleted mantle melts. In the east along the MTJ-FRSC, the lavas are dominated by flux melting resembling those at the VFR but with a strong signature of the Samoan plume [Caulfield *et al.*, 2012].

Figures 5 and 6 show two LVZs immediately beneath the MTJ-FRSC and the NWLSC-PR-LETZ, which merge to form a broader LVZ at greater depths. Such results suggest that hot mantle from the Samoan plume enters the Tonga mantle wedge within a broad flow, supplying both series of spreading centers. This is consistent with the widely distributed Samoan-plume geochemical signature in this region [Price *et al.*, 2014]. But as the mantle rises, the hot materials are confined along the spreading centers due to the focusing effect of the ridges. The relationship of these spreading centers is similar to that between the Tofua arc and the CLSC (cross section A-A'), although the lack of ANT results in this region prohibits us from further investigating the detailed shallow structure. The cross section E-E' (Figure 6) shows a connection between the PR and the removal of the Fijian lithosphere beneath the Taveuni Volcano. Given the fact that the OIB signatures have been observed in both locations [Gill and Whelan, 1989; Lytle *et al.*, 2012], this connection

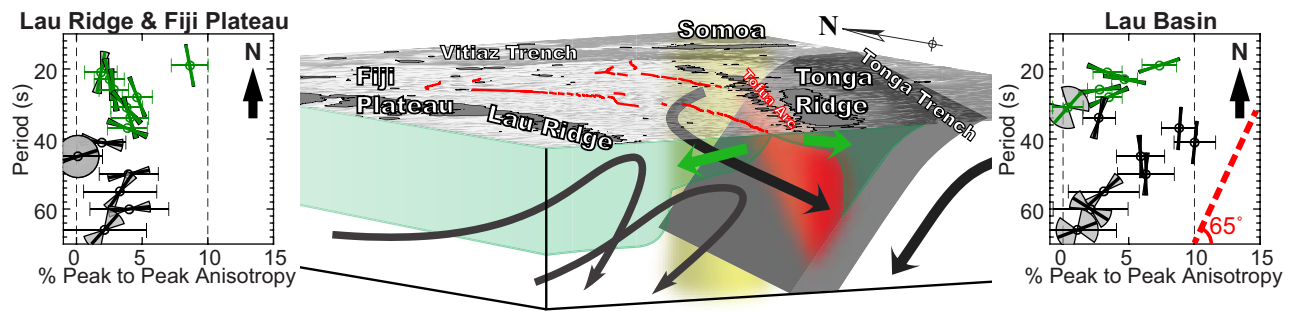


Figure 8. Conceptual explanation of the long period Rayleigh wave anisotropy results. Two insets are from Figure 2, showing anisotropy as a function of Rayleigh wave period for the Fiji Plateau-Lau Ridge (left) and the Lau Basin (right). Short bars through circles indicate the fast direction in map view (the arrow shows the direction of north in map view). Errors of fast directions are shown as gray circular sectors. Horizontal error bars display doubled standard deviations of anisotropy amplitude. Rayleigh wave period is displayed on the y axis with period increasing downward, since shorter periods are sensitive to shallower structure. The maximum sensitivity to shear velocity perturbations is located at a depth of about one-third of the wavelength, as shown in Figure 2d. Consequently, we denote the anisotropy within the lithosphere with green and anisotropy in the mantle with black, corresponding to the motion of lithosphere (green arrows) and asthenosphere (black arrows) in the schematic plot. Lithospheric anisotropy (green) is controlled by shear strain associated with the spreading process, whereas asthenospheric anisotropy (black) reflects north-south mantle flow in the Lau Basin and east-west flow farther west beneath Fiji. Red dashed line in the right inset indicates the trench orientation.

potentially reveals a mutual origin of the lavas at the NWLSC-PR-LETZ and northeastern Fiji. Due to the limited depth range resolved by the Rayleigh waves, our results are not able to distinguish between various models for the deep source of OIB signatures found in this region.

4.5. Mantle Flow: Indicated by the Seismic Anisotropy

The azimuthal anisotropy results can provide qualitative constraints on large-scale azimuthal shear wave anisotropy. In this case, we assume that the azimuthal anisotropy corresponds to the shear anisotropy at the depth of peak velocity sensitivity (Figure 2d), which given in kilometers is about $4/3$ times the period in seconds [Forsyth, 1992]. The results for the Lau Basin (Figure 2b) show that the phase velocity anisotropy beneath the Lau Basin is oriented approximately spreading-parallel (largely E-W) at periods shorter than 30 s, which sample depths shallower than about 40 km. We interpret this spreading-parallel anisotropy as resulting from lattice-preferred orientation (LPO) in upper mantle olivine caused by shear strain parallel to the spreading direction in the newborn oceanic lithosphere, which becomes frozen in as the plate ages (Figure 8). This pattern of anisotropy is similar to that found along the East Pacific Rise [Forsyth *et al.*, 1998]. The anisotropy magnitude becomes stronger and the fast direction rotates to spreading-perpendicular (mostly N-S) at periods between 30 and 55 s, corresponding to sampling depths of 40–75 km. This direction is similar to that observed by shear wave splitting and ANT studies [Smith *et al.*, 2001; Menke *et al.*, 2015], and is interpreted as indicating southward flow in the asthenosphere as a result of slab rollback and southward inflow of Samoa mantle material [Turner and Hawkesworth, 1998; Conder and Wiens, 2007; Pearce *et al.*, 2007]. Anisotropy at the longest periods, sampling deeper than 75 km, appears to be statistically unresolvable.

These observations differ somewhat from previous studies of *S*-wave splitting and ANT that consistently show trench-parallel or spreading-perpendicular anisotropy in the Lau Basin [Smith *et al.*, 2001; Menke *et al.*, 2015]. However, the *S*-wave splitting analysis only measures the accumulated anisotropy at all depths, so would be unable to resolve the relatively thin layer of spreading-parallel fast directions at depths shallower than 40 km. The ANT by Menke *et al.* [2015] was confined to 10–16 s periods (sampling depths of 13–22 km) in a small area near the ELSC, where the newborn oceanic lithosphere is expected to be less than 15 km thick. Thus the Menke *et al.* [2015] ANT results primarily sample the near-axis asthenosphere in a smaller region compared to the observations here. It is intriguing that the strongest N-S striking anisotropy is found at depths where the lowest seismic velocity is imaged, and thus where the largest melt porosity exists. So this anisotropy may also be explained as a consequence of the spreading shear strain (E-W striking), which

rotates the LPOs of partial molten rocks by 90° with respect to the shear direction due to self-organized melts [Holtzman *et al.*, 2003]. However, such mechanism requires a high melt fraction (at least $>1\%$ in average) [Hansen *et al.*, 2016], which is unlikely to exist over the whole Lau Basin. Therefore, we attribute the spreading-perpendicular anisotropy in the Lau Basin to the southward asthenosphere flow.

Beneath the Fiji Plateau and the Lau Ridge, the fast directions at periods shorter than 35 s, are oriented approximately N-S (Figure 2c). These periods sample depths shallower than 50 km, primarily in the fast, cold arc mantle lithosphere discussed in section 4.3, and presumably indicate anisotropy formed when the arc was active and later frozen in the lithosphere. It is difficult to interpret the origin of this anisotropy, because the Fiji Plateau has rotated counterclockwise by about 90° since 6.8 Ma [Malahoff *et al.*, 1982]. Anisotropy at longer periods, sampling depths deeper than 50 km, consistently strikes E-W, consistent with previous studies of S-wave splitting [Smith *et al.*, 2001]. This anisotropy has generally been interpreted as resulting from LPO caused by shear strain associated with slab induced counterflow in the asthenosphere [Karato *et al.*, 2008].

It is worthwhile to notice that the fast direction beneath the Lau Basin lithosphere is not perfectly aligned with the expected direction of the trench-parallel mantle flow. The fast axis of mantle rocks show an N-S strike with an oblique angle of about 25° with respect to the trench orientation (Figure 8), which is also observed by Menke *et al.* [2015]. One possible explanation is that the observed fast direction reflects a combined flow pattern including the along-strike corner flow (striking 205° from north) superposed by the mantle wedge corner flow perpendicular to the slab (striking 295° from north). This is supported by a quasi 3-D numerical model that imposes an along-strike flow as large as the corner flow [Marcuson *et al.*, 2014]. Alternatively, the N-S striking anisotropy may reflect the overwhelming southward flow of the Samoan plume which is not perfectly aligned with the slab. A third possibility is that our observation implies a complex history of deformation [Boneh and Skemer, 2014; Boneh *et al.*, 2015], that even if the mantle flow has been rotated from E-W striking to trench-parallel (striking 205° from north), the rotation of the LPO fast axis is lagged to striking 180° from north.

5. Conclusions

We obtained a comprehensive image of the SV-wave velocity structure of the Tonga-Lau-Fiji region by jointly inverting the Rayleigh wave phase velocities from ANT and TPWT with a Bayesian Monte-Carlo method [Shen *et al.*, 2012]. A broad LVZ is imaged in the uppermost mantle beneath the Lau Basin, indicative of hot materials upwelling from the Australian mantle in the west. Additionally, extremely low-velocity anomalies 20–80 km beneath the Lau Basin are consistent with the onset of partial melting at about 70–80 km depth. The broadly distributed melting region, along with the asymmetric mantle upwelling, shows that decompression melting is the dominant melting process in the back-arc. The Fiji Plateau and Lau Ridge ancient arc lithosphere extends down to 60–80 km depth, and is underlain by low-velocity asthenosphere. The lithosphere of the northeastern Fiji Plateau and the northern Lau Ridge may have been thinned by upwelling mantle material of plume origin.

More detailed investigations on the variations of the seismic low velocities along the spreading centers suggest that the water released from the slab significantly facilitates the melt transport and extraction at the VFR where the spreading center is much closer to the Tofua volcanic arc compared to the CLSC and ELSC in the north. The abrupt changes in geochemistry and geomorphology at about 20.6°S and 21.2°S along the ELSC-VFR result from a transition of the dominating source of mantle materials. The magmas at the CLSC and ELSC are predominantly supplied by the Australian mantle from the west, while the melt rising at the VFR mainly comes from the subduction-related mantle wedge from the east.

Results of azimuthal anisotropy show fast directions parallel to the plate spreading direction at shallow depths in the Lau Basin, which we interpret as LPO in the mantle lithosphere due to spreading processes. At deeper depths, the mantle flow direction changes from trench-perpendicular beneath the Fiji Plateau to spreading-perpendicular beneath the Lau Basin, consistent with southward flow of material from the Samoa region due to rollback of the Tonga slab.

References

- Abers, G. A., K. M. Fischer, G. Hirth, D. A. Wiens, T. Plank, B. K. Holtzman, C. McCarthy, and E. Gazel (2014), Reconciling mantle attenuation-temperature relationships from seismology, petrology, and laboratory measurements, *Geochem. Geophys. Geosyst.*, *15*, 3521–3542, doi:10.1002/2014GC005444.
- Anderson, D. L. (2007), *New Theory of the Earth*, 2nd ed., pp. 235–241, Cambridge Univ. Press, Cambridge, U. K.
- Arai, R., and R. A. Dunn (2014), Seismological study of Lau back arc crust: Mantle water, magmatic differentiation, and a compositionally zoned basin, *Earth Planet. Sci. Lett.*, *390*, 304–317, doi:10.1016/j.epsl.2014.01.014.
- Asimow, P. D., and C. H. Langmuir (2003), The importance of water to oceanic mantle melting regimes, *Nature*, *421*(6925), 815–820, doi:10.1038/nature01429.
- Barklage, M., D. A. Wiens, J. A. Conder, S. Pozgay, H. Shiobara, and H. Sugioka (2015), P and S velocity tomography of the Mariana subduction system from a combined land-sea seismic deployment, *Geochem. Geophys. Geosyst.*, *16*, 681–704, doi:10.1002/2014GC005627.
- Bell, S. W., D. W. Forsyth, and Y. Ruan (2015), Removing noise from the vertical component records of ocean-bottom seismometers: Results from year one of the Cascadia Initiative, *Bull. Seismol. Soc. Am.*, *105*(1), 300–313, doi:10.1785/0120140054.
- Bézos, A., S. Escrig, C. H. Langmuir, P. J. Michael, and P. D. Asimow (2009), Origins of chemical diversity of back-arc basin basalts: A segment-scale study of the Eastern Lau Spreading Center, *J. Geophys. Res.*, *114*, B06212, doi:10.1029/2008JB005924.
- Boneh, Y., and P. Skemer (2014), The effect of deformation history on the evolution of olivine CPO, *Earth Planet. Sci. Lett.*, *406*, 213–222, doi:10.1016/j.epsl.2014.09.018.
- Boneh, Y., L. F. G. Morales, E. Kaminski, and P. Skemer (2015), Modeling olivine CPO evolution with complex deformation histories: Implications for the interpretation of seismic anisotropy in the mantle, *Geochem. Geophys. Geosyst.*, *16*, 3436–3455, doi:10.1002/2015GC005964.
- Caulfield, J., S. Turner, R. Arculus, C. Dale, F. Jenner, J. Pearce, C. Macpherson, and H. Handley (2012), Mantle flow, volatiles, slab-surface temperatures and melting dynamics in the north Tonga arc-Lau back-arc basin, *J. Geophys. Res.*, *117*, B11209, doi:10.1029/2012JB009526.
- Chen, J., D. A. Wiens, S. S. Wei, Y. Zha, J. Julià, C. Cai, and Y. J. Chen (2015), The crustal thickness and lithospheric structure of active and inactive volcanic arc terrains in Fiji and Tonga, Abstract S13A-2783 presented at 2015 AGU Fall Meeting, AGU, San Francisco, Calif.
- Conder, J. A., and D. A. Wiens (2006), Seismic structure beneath the Tonga arc and Lau back-arc basin determined from joint Vp, Vp/Vs tomography, *Geochem. Geophys. Geosyst.*, *7*, Q03018, doi:10.1029/2005GC001113.
- Conder, J. A., and D. A. Wiens (2007), Rapid mantle flow beneath the Tonga volcanic arc, *Earth Planet. Sci. Lett.*, *264*(1–2), 299–307, doi:10.1016/j.epsl.2007.10.014.
- Conder, J. A., D. A. Wiens, and J. Morris (2002), On the decompression melting structure at volcanic arcs and back-arc spreading centers, *Geophys. Res. Lett.*, *29*(15), 1727, doi:10.1029/2002GL015390.
- Crawford, W. C., and S. C. Webb (2000), Identifying and removing tilt noise from low-frequency (<0.1 Hz) seafloor vertical seismic data, *Bull. Seismol. Soc. Am.*, *90*(4), 952–963, doi:10.1785/0119990121.
- Crawford, W. C., J. A. Hildebrand, L. M. Dorman, S. C. Webb, and D. A. Wiens (2003), Tonga Ridge and Lau Basin crustal structure from seismic refraction data, *J. Geophys. Res.*, *108*(B4), 2195, doi:10.1029/2001JB001435.
- Dubois, J., G. Pascal, M. Barazangi, B. L. Isacks, and J. Oliver (1973), Travel times of seismic waves between the New Hebrides and Fiji Islands: A zone of low velocity beneath the Fiji Plateau, *J. Geophys. Res.*, *78*(17), 3431–3436, doi:10.1029/JB078i017p03431.
- Dunn, R. A., and F. Martinez (2011), Contrasting crustal production and rapid mantle transitions beneath back-arc ridges, *Nature*, *469*(7329), 198–202, doi:10.1038/nature09690.
- Dunn, R. A., F. Martinez, and J. A. Conder (2013), Crustal construction and magma chamber properties along the Eastern Lau Spreading Center, *Earth Planet. Sci. Lett.*, *371*–372, 112–124, doi:10.1016/j.epsl.2013.04.008.
- Ekström, G., G. A. Abers, and S. C. Webb (2009), Determination of surface-wave phase velocities across USArray from noise and Aki's spectral formulation, *Geophys. Res. Lett.*, *36*, L18301, doi:10.1029/2009GL039131.
- Escrig, S., A. Bézos, S. L. Goldstein, C. H. Langmuir, and P. J. Michael (2009), Mantle source variations beneath the Eastern Lau Spreading Center and the nature of subduction components in the Lau basin-Tonga arc system, *Geochem. Geophys. Geosyst.*, *10*, Q04014, doi:10.1029/2008GC002281.
- Falloon, T. J., A. Malahoff, L. P. Zonenshaina, and Y. Bogdanova (1992), Petrology and geochemistry of back-arc basin basalts from Lau Basin spreading ridges at 15°, 18° and 19°S, *Mineral. Petrol.*, *47*(1), 1–35, doi:10.1007/BF01165295.
- Faul, U., and I. Jackson (2015), Transient creep and strain energy dissipation: An experimental perspective, *Annu. Rev. Earth Planet. Sci.*, *43*(1), 541–569, doi:10.1146/annurev-earth-060313-054732.
- Faul, U. H., and I. Jackson (2005), The seismological signature of temperature and grain size variations in the upper mantle, *Earth Planet. Sci. Lett.*, *234*(1–2), 119–134.
- Faul, U. H., J. D. Fitz Gerald, and I. Jackson (2004), Shear wave attenuation and dispersion in melt-bearing olivine polycrystals: 2. Microstructural interpretation and seismological implications, *J. Geophys. Res.*, *109*, B06202, doi:10.1029/2003JB002407.
- Forsyth, D. W. (1992), Geophysical constraints on mantle flow and melt generation beneath mid-ocean ridges, in *Mantle Flow and Melt Generation at Mid-Ocean Ridges*, edited by J. P. Morgan, et al., pp. 1–65, AGU, Washington, D. C.
- Forsyth, D. W., and A. Li (2005), Array analysis of two-dimensional variations in surface wave phase velocity and azimuthal anisotropy in the presence of multipathing interference, in *Seismic Earth: Array Analysis of Broadband Seismograms*, edited by A. Levander and G. Nolet, pp. 81–97, AGU, Washington, D. C.
- Forsyth, D. W., S. C. Webb, L. M. Dorman, and Y. Shen (1998), Phase velocities of Rayleigh waves in the MELT experiment on the East Pacific Rise, *Science*, *280*(5367), 1235–1238, doi:10.1126/science.280.5367.1235.
- Gill, J., and P. Whelan (1989), Postsubduction Ocean Island Alkali Basalts in Fiji, *J. Geophys. Res.*, *94*(B4), 4579–4588, doi:10.1029/JB094iB04p04579.
- Goes, S., J. Armitage, N. Harmon, H. Smith, and R. Huisman (2012), Low seismic velocities below mid-ocean ridges: Attenuation versus melt retention, *J. Geophys. Res.*, *117*, B12403, doi:10.1029/2012JB009637.
- Hammond, W. C., and E. D. Humphreys (2000a), Upper mantle seismic wave velocity: Effects of realistic partial melt geometries, *J. Geophys. Res.*, *105*(B5), 10,975–10,986, doi:10.1029/2000JB900041.
- Hammond, W. C., and E. D. Humphreys (2000b), Upper mantle seismic wave attenuation: Effects of realistic partial melt distribution, *J. Geophys. Res.*, *105*(B5), 10,987–10,999, doi:10.1029/2000JB900042.
- Hansen, L. N., C. Qi, and J. M. Warren (2016), Olivine anisotropy suggests Gutenberg discontinuity is not the base of the lithosphere, *Proc. Natl. Acad. Sci. U. S. A.*, *113*(38), 10,503–10,506, doi:10.1073/pnas.1608269113.

- Harmon, N., and D. K. Blackman (2010), Effects of plate boundary geometry and kinematics on mantle melting beneath the back-arc spreading centers along the Lau Basin, *Earth Planet. Sci. Lett.*, *298*(3–4), 334–346, doi:10.1016/j.epsl.2010.08.004.
- Hayes, G. P., D. J. Wald, and R. L. Johnson (2012), Slab1.0: A three-dimensional model of global subduction zone geometries, *J. Geophys. Res.*, *117*, B01302, doi:10.1029/2011JB008524.
- Herrmann, R. B. (2004), *Computer Programs in Seismology*, Earthquake Cent., Saint Louis Univ., St. Louis.
- Hirschmann, M. M., C. Aubaud, and A. C. Withers (2005), Storage capacity of H₂O in nominally anhydrous minerals in the upper mantle, *Earth Planet. Sci. Lett.*, *236*(1–2), 167–181, doi:10.1016/j.epsl.2005.04.022.
- Hirth, G., and D. L. Kohlstedt (1996), Water in the oceanic upper mantle: Implications for rheology, melt extraction and the evolution of the lithosphere, *Earth Planet. Sci. Lett.*, *144*(1–2), 93–108, doi:10.1016/0012-821x(96)00154-9.
- Holtzman, B. K. (2016), Questions on the existence, persistence, and mechanical effects of a very small melt fraction in the asthenosphere, *Geochem. Geophys. Geosyst.*, *17*, 470–484, doi:10.1002/2015GC006102.
- Holtzman, B. K., D. L. Kohlstedt, M. E. Zimmerman, F. Heidelbach, T. Hiraga, and J. Hustoft (2003), Melt segregation and strain partitioning: Implications for seismic anisotropy and mantle flow, *Science*, *301*(5637), 1227–1230, doi:10.1126/science.1087132.
- Isaak, D. G. (1992), High-temperature elasticity of iron-bearing olivines, *J. Geophys. Res.*, *97*(B2), 1871–1885, doi:10.1029/91JB02675.
- Jackson, I., and U. H. Faul (2010), Grain-size-sensitive viscoelastic relaxation in olivine: Towards a robust laboratory-based model for seismological application, *Phys. Earth Planet. Inter.*, *183*(1–2), 151–163.
- Kanamori, H., and D. L. Anderson (1977), Importance of physical dispersion in surface wave and free oscillation problems: Review, *Rev. Geophys.*, *15*(1), 105–112, doi:10.1029/RG015i001p00105.
- Karato, S.-I. (1993), Importance of anelasticity in the interpretation of seismic tomography, *Geophys. Res. Lett.*, *20*(15), 1623–1626, doi:10.1029/93GL01767.
- Karato, S.-I. (2003), Mapping water content in the upper mantle, in *Inside the Subduction Factory*, edited by J. M. Eiler, pp. 135–152, AGU, Washington, D. C.
- Karato, S.-I. (2012), On the origin of the asthenosphere, *Earth Planet. Sci. Lett.*, *321*–322, 95–103, doi:10.1016/j.epsl.2012.01.001.
- Karato, S.-I., H. Jung, I. Katayama, and P. Skemer (2008), Geodynamic significance of seismic anisotropy of the Upper Mantle: New insights from laboratory studies, *Annu. Rev. Earth Planet. Sci.*, *36*(1), 59–95, doi:10.1146/annurev.earth.36.031207.124120.
- Kelley, K. A., T. Plank, T. L. Grove, E. M. Stolper, S. Newman, and E. Hauri (2006), Mantle melting as a function of water content beneath back-arc basins, *J. Geophys. Res.*, *111*, B09208, doi:10.1029/2005JB003732.
- Koper, K. D., D. A. Wiens, L. M. Dorman, J. A. Hildebrand, and S. C. Webb (1998), Modeling the Tonga slab: Can travel time data resolve a metastable olivine wedge?, *J. Geophys. Res.*, *103*(B12), 30,079–30,100, doi:10.1029/98JB01517.
- Lee, C.-T. A. (2003), Compositional variation of density and seismic velocities in natural peridotites at STP conditions: Implications for seismic imaging of compositional heterogeneities in the upper mantle, *J. Geophys. Res.*, *108*(B9), 2441, doi:10.1029/2003JB002413.
- Lee, C.-T. A., P. Luffi, T. Plank, H. Dalton, and W. P. Leeman (2009), Constraints on the depths and temperatures of basaltic magma generation on Earth and other terrestrial planets using new thermobarometers for mafic magmas, *Earth Planet. Sci. Lett.*, *279*(1–2), 20–33, doi:10.1016/j.epsl.2008.12.020.
- Lindquist, K. G., K. Engle, D. Stahlke, and E. Price (2004), Global topography and bathymetry grid improves research efforts, *Eos Trans. AGU*, *85*(19), 186–186, doi:10.1029/2004EO190003.
- Lytle, M. L., K. A. Kelley, E. H. Hauri, J. B. Gill, D. Papia, and R. J. Arculus (2012), Tracing mantle sources and Samoan influence in the north-western Lau back-arc basin, *Geochem. Geophys. Geosyst.*, *13*, Q10019, doi:10.1029/2012GC004233.
- Malahoff, A., S. R. Hammond, J. J. Naughton, D. L. Keeling, and R. N. Richmond (1982), Geophysical evidence for post-Miocene rotation of the island of Viti Levu, Fiji, and its relationship to the tectonic development of the North Fiji Basin, *Earth Planet. Sci. Lett.*, *57*(2), 398–414, doi:10.1016/0012-821x(82)90159-5.
- Marcuson, R., D. K. Blackman, and N. Harmon (2014), Seismic anisotropy predicted for 2-D plate-driven flow in the Lau back-arc basin, *Phys. Earth Planet. Inter.*, *233*, 88–94, doi:10.1016/j.pepi.2014.06.007.
- Martinez, F., and B. Taylor (2002), Mantle wedge control on back-arc crustal accretion, *Nature*, *416*(6879), 417–420, doi:10.1038/416417a.
- Martinez, F., B. Taylor, E. T. Baker, J. A. Resing, and S. L. Walker (2006), Opposing trends in crustal thickness and spreading rate along the back-arc Eastern Lau Spreading Center: Implications for controls on ridge morphology, faulting, and hydrothermal activity, *Earth Planet. Sci. Lett.*, *245*(3–4), 655–672, doi:10.1016/j.epsl.2006.03.049.
- McCarthy, C., and Y. Takei (2011), Anelasticity and viscosity of partially molten rock analogue: Toward seismic detection of small quantities of melt, *Geophys. Res. Lett.*, *38*, L18306, doi:10.1029/2011GL048776.
- McCarthy, C., Y. Takei, and T. Hiraga (2011), Experimental study of attenuation and dispersion over a broad frequency range: 2. The universal scaling of polycrystalline materials, *J. Geophys. Res.*, *116*, B09207, doi:10.1029/2011JB008384.
- Menke, W., Y. Zha, S. C. Webb, and D. K. Blackman (2015), Seismic anisotropy indicates ridge-parallel asthenospheric flow beneath the Eastern Lau Spreading Center, *J. Geophys. Res. Solid Earth*, *120*, 976–992, doi:10.1002/2014JB011154.
- Miller, K. J., W.-I. Zhu, L. G. J. Montési, and G. A. Gaetani (2014), Experimental quantification of permeability of partially molten mantle rock, *Earth Planet. Sci. Lett.*, *388*, 273–282, doi:10.1016/j.epsl.2013.12.003.
- Montagner, J.-P., and H.-C. Nataf (1986), A simple method for inverting the azimuthal anisotropy of surface waves, *J. Geophys. Res.*, *91*(B1), 511–520, doi:10.1029/JB091iB01p00511.
- Nishimura, C. E., and D. W. Forsyth (1989), The anisotropic structure of the upper mantle in the Pacific, *Geophys. J. Int.*, *96*(2), 203–229, doi:10.1111/j.1365-246X.1989.tb04446.x.
- Pearce, J. A., M. Ernewein, S. H. Bloomer, L. M. Parson, B. J. Murton, and L. E. Johnson (1994), Geochemistry of Lau Basin volcanic rocks: Influence of ridge segmentation and arc proximity, *Geol. Soc. Spec. Publ.*, *81*(1), 53–75, doi:10.1144/gsl.sp.1994.081.01.04.
- Pearce, J. A., P. D. Kempton, and J. B. Gill (2007), Hf-Nd evidence for the origin and distribution of mantle domains in the SW Pacific, *Earth Planet. Sci. Lett.*, *260*(1–2), 98–114, doi:10.1016/j.epsl.2007.05.023.
- Phipps Morgan, J. (1997), The generation of a compositional lithosphere by mid-ocean ridge melting and its effect on subsequent off-axis hotspot upwelling and melting, *Earth Planet. Sci. Lett.*, *146*(1–2), 213–232, doi:10.1016/S0012-821X(96)00207-5.
- Price, A. A., M. G. Jackson, J. Blichert-Toft, P. S. Hall, J. M. Sinton, M. D. Kurz, and J. Blusztajn (2014), Evidence for a broadly distributed Samoan-plume signature in the northern Lau and North Fiji Basins, *Geochem. Geophys. Geosyst.*, *15*, 986–1008, doi:10.1002/2013GC005061.
- Rau, C. J., and D. W. Forsyth (2011), Melt in the mantle beneath the amagmatic zone, southern Nevada, *Geology*, *39*(10), 975–978, doi:10.1130/g32179.1.
- Roth, E. G., D. A. Wiens, L. M. Dorman, J. Hildebrand, and S. C. Webb (1999), Seismic attenuation tomography of the Tonga-Fiji region using phase pair methods, *J. Geophys. Res.*, *104*(B3), 4795–4809, doi:10.1029/1998JB900052.

- Schutt, D. L., and C. E. Lesher (2010), Compositional trends among Kaapvaal Craton garnet peridotite xenoliths and their effects on seismic velocity and density, *Earth Planet. Sci. Lett.*, *300*(3–4), 367–373, doi:10.1016/j.epsl.2010.10.018.
- Shen, W., M. H. Ritzwoller, V. Schulte-Pelkum, and F.-C. Lin (2012), Joint inversion of surface wave dispersion and receiver functions: A Bayesian Monte-Carlo approach, *Geophys. J. Int.*, *192*, 807–836, doi:10.1093/gji/ggs050.
- Shen, W., M. H. Ritzwoller, and V. Schulte-Pelkum (2013), A 3-D model of the crust and uppermost mantle beneath the Central and Western US by joint inversion of receiver functions and surface wave dispersion, *J. Geophys. Res.*, *118*, 262–276, doi:10.1029/2012JB009602.
- Shen, Y., and D. W. Forsyth (1995), Geochemical constraints on initial and final depths of melting beneath mid-ocean ridges, *J. Geophys. Res.*, *100*(B2), 2211–2237, doi:10.1029/94JB02768.
- Smith, G. P., D. A. Wiens, K. M. Fischer, L. M. Dorman, S. C. Webb, and J. A. Hildebrand (2001), A complex pattern of mantle flow in the Lau backarc, *Science*, *292*(5517), 713–716, doi:10.1126/science.1058763.
- Sparks, D. W., and E. M. Parmentier (1993), The structure of three-dimensional convection beneath oceanic spreading centres, *Geophys. J. Int.*, *112*(1), 81–91, doi:10.1111/j.1365-246X.1993.tb01438.x.
- Sundberg, M., and R. F. Cooper (2010), A composite viscoelastic model for incorporating grain boundary sliding and transient diffusion creep: correlating creep and attenuation responses for materials with a fine grain size, *Philos. Mag.*, *90*(20), 2817–2840, doi:10.1080/14786431003746656.
- Takei, Y. (2002), Effect of pore geometry on VP/VS: From equilibrium geometry to crack, *J. Geophys. Res.*, *107*(B2), 2043, doi:10.1029/2001JB000522.
- Taylor, B., K. Zellmer, F. Martinez, and A. Goodliffe (1996), Sea-floor spreading in the Lau back-arc basin, *Earth Planet. Sci. Lett.*, *144*(1–2), 35–40, doi:10.1016/0012-821x(96)00148-3.
- The MELT Seismic Team (1998), Imaging the deep seismic structure beneath a mid-ocean ridge: The MELT experiment, *Science*, *280*(5367), 1215–1218, doi:10.1126/science.280.5367.1215.
- Turner, I. M., C. Peirce, and M. C. Sinha (1999), Seismic imaging of the axial region of the Valu Fa Ridge, Lau Basin—The accretionary processes of an intermediate back-arc spreading ridge, *Geophys. J. Int.*, *138*(2), 495–519, doi:10.1046/j.1365-246X.1999.00883.x.
- Turner, S., and C. Hawkesworth (1998), Using geochemistry to map mantle flow beneath the Lau Basin, *Geology*, *26*(11), 1019–1022, doi:10.1130/0091-7613(1998)026 < 1019:ugtmf > 2.3.co;2.
- Webb, S. C., and W. C. Crawford (1999), Long-period seafloor seismology and deformation under ocean waves, *Bull. Seismol. Soc. Am.*, *89*(6), 1535–1542.
- Wei, S. S. (2016), *Seismic Studies of the Tonga Subduction Zone and the Lau Back-Arc Basin*, 188 pp., Washington Univ., St. Louis.
- Wei, S. S., D. A. Wiens, Y. Zha, T. Plank, S. C. Webb, D. K. Blackman, R. A. Dunn, and J. A. Conder (2015), Seismic evidence of effects of water on melt transport in the Lau back-arc mantle, *Nature*, *518*(7539), 395–398, doi:10.1038/nature14113.
- Wendt, J. I., M. Regelous, K. D. Collerson, and A. Ewart (1997), Evidence for a contribution from two mantle plumes to island-arc lavas from northern Tonga, *Geology*, *25*(7), 611–614, doi:10.1130/0091-7613(1997)025 < 0611:efact > 2.3.co;2.
- Wiens, D. A., K. A. Kelley, and T. Plank (2006), Mantle temperature variations beneath back-arc spreading centers inferred from seismology, petrology, and bathymetry, *Earth Planet. Sci. Lett.*, *248*(1–2), 30–42.
- Wiens, D. A., J. A. Conder, and U. H. Faul (2008), The seismic structure and dynamics of the mantle wedge, *Annu. Rev. Earth Planet. Sci.*, *36*(1), 421–455, doi:10.1146/annurev.earth.33.092203.122633.
- Yang, Y., and D. W. Forsyth (2006), Regional tomographic inversion of the amplitude and phase of Rayleigh waves with 2-D sensitivity kernels, *Geophys. J. Int.*, *166*(3), 1148–1160, doi:10.1111/j.1365-246X.2006.02972.x.
- Yang, Y., M. H. Ritzwoller, F. C. Lin, M. P. Moschetti, and N. M. Shapiro (2008), Structure of the crust and uppermost mantle beneath the western United States revealed by ambient noise and earthquake tomography, *J. Geophys. Res.*, *113*, B12310, doi:10.1029/2008JB005833.
- Yao, H., R. D. van Der Hilst, and M. V. de Hoop (2006), Surface-wave array tomography in SE Tibet from ambient seismic noise and two-station analysis—I. Phase velocity maps, *Geophys. J. Int.*, *166*(2), 732–744, doi:10.1111/j.1365-246X.2006.03028.x.
- Yoshizawa, K., and B. L. N. Kennett (2002), Determination of the influence zone for surface wave paths, *Geophys. J. Int.*, *149*(2), 440–453, doi:10.1046/j.1365-246X.2002.01659.x.
- Zellmer, K. E., and B. Taylor (2001), A three-plate kinematic model for Lau Basin opening, *Geochem. Geophys. Geosyst.*, *2*(5), 1020, doi:10.1029/2000GC000106.
- Zha, Y., S. C. Webb, S. S. Wei, D. A. Wiens, D. K. Blackman, W. Menke, R. A. Dunn, and J. A. Conder (2014), Seismological imaging of ridge-arc interaction beneath the Eastern Lau Spreading Center from OBS ambient noise tomography, *Earth Planet. Sci. Lett.*, *408*, 194–206, doi:10.1016/j.epsl.2014.10.019.
- Zhao, D., Y. Xu, D. A. Wiens, L. Dorman, J. Hildebrand, and S. Webb (1997), Depth extent of the Lau back-arc spreading center and its relation to subduction processes, *Science*, *278*(5336), 254–257, doi:10.1126/science.278.5336.254.